Resource

Cell Reports

Dissecting Sholl Analysis into Its Functional Components

Graphical Abstract

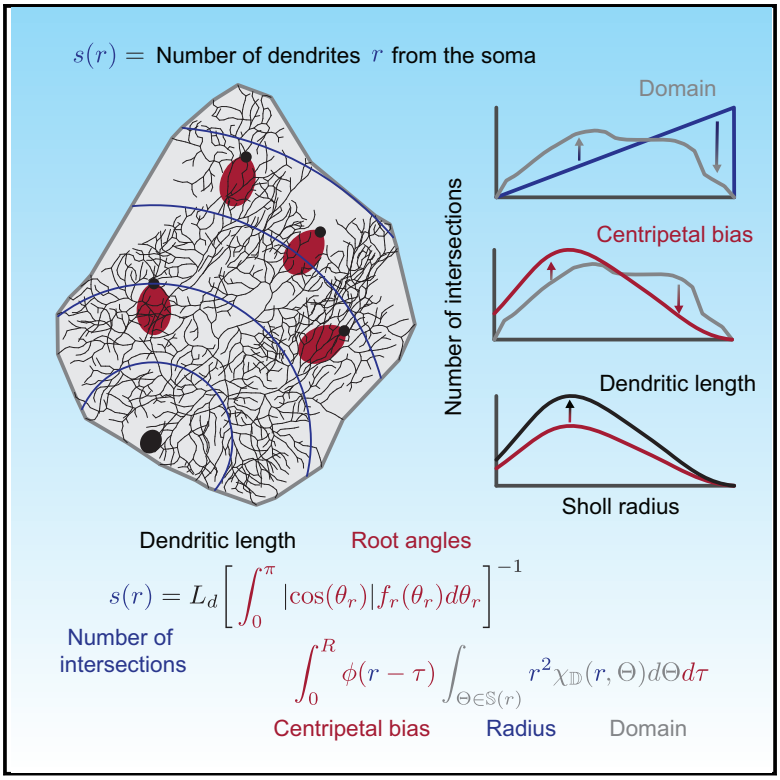

Authors

Alex D. Bird, Hermann Cuntz

Correspondence

bird@fias.uni-frankfurt.de

In Brief

Bird and Cuntz show how Sholl analysis, a one-dimensional representation of a dendritic tree, can be reproduced from three basic properties of a neuron that define its connectivity, density of synaptic inputs, and balance between material and signal delay costs, thus linking an intuitive and accessible neuronal representation with function.

Highlights

- Root angle measure quantifies a dendrite's centripetal bias
- Functional interpretation of dendrites without full reconstruction
- Parameter estimation for optimal wiring-based dendrite models
- Simple relation between dendrite length and Sholl profile

Bird & Cuntz, 2019, Cell Reports *27*, 3081–3096
June 4, 2019 © 2019 The Author(s).
https://doi.org/10.1016/j.celrep.2019.04.097

CellPress

Cell Reports
Resource

OPEN ACCESS
CellPress

Dissecting Sholl Analysis into Its Functional Components

Alex D. Bird[1,2,3,*] and Hermann Cuntz[1,2]
[1]Frankfurt Institute for Advanced Studies, Frankfurt-am-Main 60438, Germany
[2]Ernst Strüngmann Institute (ESI) for Neuroscience in Cooperation with Max Planck Society, Frankfurt-am-Main 60528, Germany
[3]Lead Contact
*Correspondence: bird@fias.uni-frankfurt.de
https://doi.org/10.1016/j.celrep.2019.04.097

SUMMARY

Sholl analysis has been an important technique in dendritic anatomy for more than 60 years. The Sholl intersection profile is obtained by counting the number of dendritic branches at a given distance from the soma and is a key measure of dendritic complexity; it has applications from evaluating the changes in structure induced by pathologies to estimating the expected number of anatomical synaptic contacts. We find that the Sholl intersection profiles of most neurons can be reproduced from three basic, functional measures: the domain spanned by the dendritic arbor, the total length of the dendrite, and the angular distribution of how far dendritic segments deviate from a direct path to the soma (i.e., the root angle distribution). The first two measures are determined by axon location and hence microcircuit structure; the third arises from optimal wiring and represents a branching statistic estimating the need for conduction speed in a neuron.

INTRODUCTION

Neuronal morphologies are diverse, with great variation among individual cells, classes of cells, and similar cells in different animal species. The structure of a neuron's dendritic tree defines how the cell can receive synaptic inputs from other neurons and strongly influences how these inputs are integrated to allow signal transmission and computation. Dendritic trees are surprisingly hard to describe precisely, and this makes comparative studies of the structure or function of a dendrite fraught with difficulty. Sholl analysis has established itself as a widely used method of evaluating neuronal morphologies (Ascoli et al., 2008; Langhammer et al., 2010; Binley et al., 2014; Ferreira et al., 2014; Gutierrez and Davies, 2007; Johnson et al., 2016; Keil et al., 2017; Wilson et al., 2017) since its introduction in 1953 by Donald Sholl (Sholl, 1953). The Sholl intersection profile (SIP) $s(r)$ counts the number of times a dendrite intersects an imaginary sphere of a given radius r centered on the soma; it therefore gives a one-dimensional representation of the complexity of the three-dimensional dendrite. This reduction in dimensionality allows for intuitive comparisons of complex dendritic structures (O'Keeffe et al., 2008; Ascoli et al., 2008; Williams et al., 2013) and thus has major applications across neuroscience. Links have been made between SIP and dendritic function; the SIP can define the expected number of synaptic contacts (Liley and Wright, 1994) or, if taking non-uniform dendritic diameter into account, illustrate morphological influence on action potential backpropagation (Vetter et al., 2001). Fractal measures of neuronal morphology (Smith et al., 1989; Caserta et al., 1990), which quantify how well a dendrite fills its space, have also been shown to correlate strongly with statistics derived from the SIP (Caserta et al., 1995; Fernández and Jelinek, 2001). Most recently, SIPs have been widely used to demonstrate changes in neuronal structure caused by genetic manipulation (O'Keeffe et al., 2008; Peng et al., 2015), pathology (Williams et al., 2013; Chittajallu et al., 2017), or treatment (Kigerl et al., 2009; Rekha et al., 2011).

The SIP can be reliably computed automatically from noisy raw image stacks (Kutzing et al., 2010; Ferreira et al., 2014), meaning that large-scale imaging studies are able to recover many SIPs (Rekha et al., 2011; Chittajallu et al., 2017) without the difficulties of fully reconstructing the morphologies (Donohue and Ascoli, 2011; Radojević and Meijering, 2017). With increases in the usage of relatively high-throughput imaging techniques (Wu et al., 2004; Gong et al., 2016), the SIP is likely to remain an important metric when assessing neuronal morphology across both theoretical and experimental neuroscience.

Despite its broad usage, the interpretation of the SIP remains largely qualitative and typically lacks comprehensive insight into the functional factors that lead to a given SIP. Work continues to improve (Ristanović et al., 2006; O'Neill et al., 2015) and interpret (Garcia-Segura and Perez-Marquez, 2014; Rajković et al., 2016; Wilson et al., 2017) this key measure of neuronal structure. In this study, we provide a framework to assess the SIP of a given neuron or neuronal class by estimating the profile from basic morphological properties with direct functional interpretations.

We show that SIPs can be approximated by three basic, functional measures: the domain spanned by the dendritic arbor, the total length of the dendrite, and the angular distribution of how far dendritic segments deviate from a direct path to the soma (which we quantify with a metric called the root angle). The first two measures are principally determined by axon location and abundance, and hence microcircuit structure (Chklovskii, 2004); the third arises from the balance between total dendritic length and path length from synapses to the soma (Cuntz et al., 2010). For many cell classes, the SIP can be closely approximated by considering just these three basic factors.

This is an open access article under the CC BY license (http://creativecommons.org/licenses/by/4.0/).

Table 1. Table Summarizing Symbols and Terms

Symbol	Interpretation
A_s	scale (integral) of SIP (μm)
α	fitted shrink factor (1 − convexity)
bf	balancing factor
$\mathbb{D}$	domain spanned by dendrites
$f_{r,2}(\theta_r)$	root angle distribution for planar neurons
$f_{r,3}(\theta_r)$	root angle distribution for three-dimensional neurons
θ_r	root angle (rad)
κ	von Mises bias parameter
L_d	total dendritic length (μm)
r	radial distance from soma (μm)
$\rho(r)$	radial density of planar dendrite (μm)
$s(r)$	(true) Sholl intersection profile (SIP)
$s_d(r)$	domain-based SIP approximation (Equation 1)
$s_\rho(r)$	density-based SIP approximation (Equation 2)
$s_r(r)$	root angle-based SIP approximation (Equation 6)
$\mathbb{S}(r)$	sphere of radius r centered on the soma
$\phi(x)$	root angle distribution as a function of distance

RESULTS

Predicting Sholl Profiles from Dendrite Spanning Fields

Dendrites cover a specific region, and they fill space with varying degrees of compactness (Montague and Friedlander, 1991; Ristanović et al., 2009; Snider et al., 2010). If we denote this region $\mathbb{D}$, a first proportional approximation $s_d(r)$ to the true SIP $s(r)$ can be given by the intersection of a sphere $\mathbb{S}(r)$ of radius r with $\mathbb{D}$:

$$s_d(r) = \int_{\Theta \in \mathbb{S}(r)} r^2 \chi_{\mathbb{D}}(r,\Theta) d\Theta, \qquad \text{(Equation 1)}$$

where Θ is a point on $\mathbb{S}(r)$ and $\chi_{\mathbb{D}}(r,\Theta)$ is the indicator function for point (r,Θ) in $\mathbb{D}$. All terms are summarized in Table 1. For planar neurons, the r^2 in the integral becomes r. Figure 1A provides an illustration of this method on a cerebellar Purkinje cell, with $\mathbb{D}$ indicated by gray shading and $\mathbb{S}(r)$ indicated in black for several values of r.

Convex Spanning Fields

The most straightforward application of this approach is to neurons that are relatively convex. Here the spanning field $\mathbb{D}$ can be described by the convex hull of the dendrite (Figure 1A, gray). Many classes of planar neuron have this characteristic, in particular cerebellar Purkinje cells (Figures 1A and 1B), several fly neurons (Figure 1C), and many retinal cells (Figure 1D). The comparison of the true SIP (Figure 1, black lines) with that predicted by the convex spanning field with Equation 1 (Figures 1A–1D, gray shading) shows a close match for these example cells. The predictive power of Equation 1 can be quantified using the normalized root-mean-square deviation of the estimated SIP from the measured value (see STAR Methods and Figure S1).

Non-convex Spanning Fields

The domain-based prediction can be simply extended to neurons with non-convex spanning fields. An example of this for planar cells would be a fly vertical system (VS) neuron (Figures 1E and 1F), but the issue becomes more important in three dimensions (Figure 1G), in which the simple convex hull can provide a poor match to the volume covered by the dendritic tree. In these cases, it is necessary to define $\mathbb{D}$ more carefully (see STAR Methods and Figure S2).

The improved definition of $\mathbb{D}$ relies on the concept of α shapes (Edelsbrunner et al., 1983), which generalize the idea of a convex hull by defining a boundary between a pure convex hull and the tightest connected boundary around a structure; the construction relies on a single parameter between 0 and 1, which we derive from a measure of the convexity of the neuron (see STAR Methods and Table S2). $\mathbb{D}$ for non-convex spanning fields is shown in Figure 1 for planar cells (Figures 1E and 1F, pink shading line against the pure convex hull gray) and for a neuron with a three-dimensional structure (Figure 1G). Using the improved definition increases the accuracy of the estimate given by Equation 1 (Figure S2F).

Overall, the approximation from Equation 1 with the correct definition of the dendritic spanning field $\mathbb{D}$ corresponds well to the observed SIPs of many classes of neuron. This is due to a relative uniformity of dendritic structure as assumed by Equation 1; the expected density of the dendritic cable does not appear to change with distance from the soma for these classes of cell.

Limitations of the Dendrite Spanning Field as a Predictor for SIPs

The fundamental assumption of the domain-based SIP approximation is that the density of the dendrite within the spanning field is approximately constant. This assumption allows accurate estimation of SIPs in numerous cases (Figure 1), but it is not necessarily true. The most straightforward deviation from this case arises when the density of the dendrite has marked asymmetry along radii. This can be seen in the case of the starburst amacrine cell (Figure 2A, upper left panel); the density of the dendrite sharply increases in the most distal portion, and this leads to a distal shift in the true SIP compared to that predicted by the domain alone (Figure 2A, lower left panel). In contrast, a cerebellar Purkinje cell (Figure 2A, upper right panel), which is well described by the spanning field, can have some local non-uniformities, but these average out and do not substantially alter the SIP predicted by Equation 1. In the case of the starburst amacrine cell, the deviation correlates with the known retinal circuit structure: the neuron receives synapses across its dendritic tree but also forms inhibitory synapses onto neighboring cells in approximately the most distal third of its dendritic tree (Famiglietti, 1991). Increasing (in the case of the amacrine cell, doubling) the predicted density $\rho(r)$ of the dendrite in this region allows a more accurate estimation of the true SIP:

$$s_\rho(r) = \int_{\Theta \in \mathbb{S}(r)} r\rho(r)\chi_{\mathbb{D}}(r,\Theta) d\Theta \qquad \text{(Equation 2)}$$

Although a straightforward non-uniformity in dendritic density may reveal specific aspects of local circuit structure and be

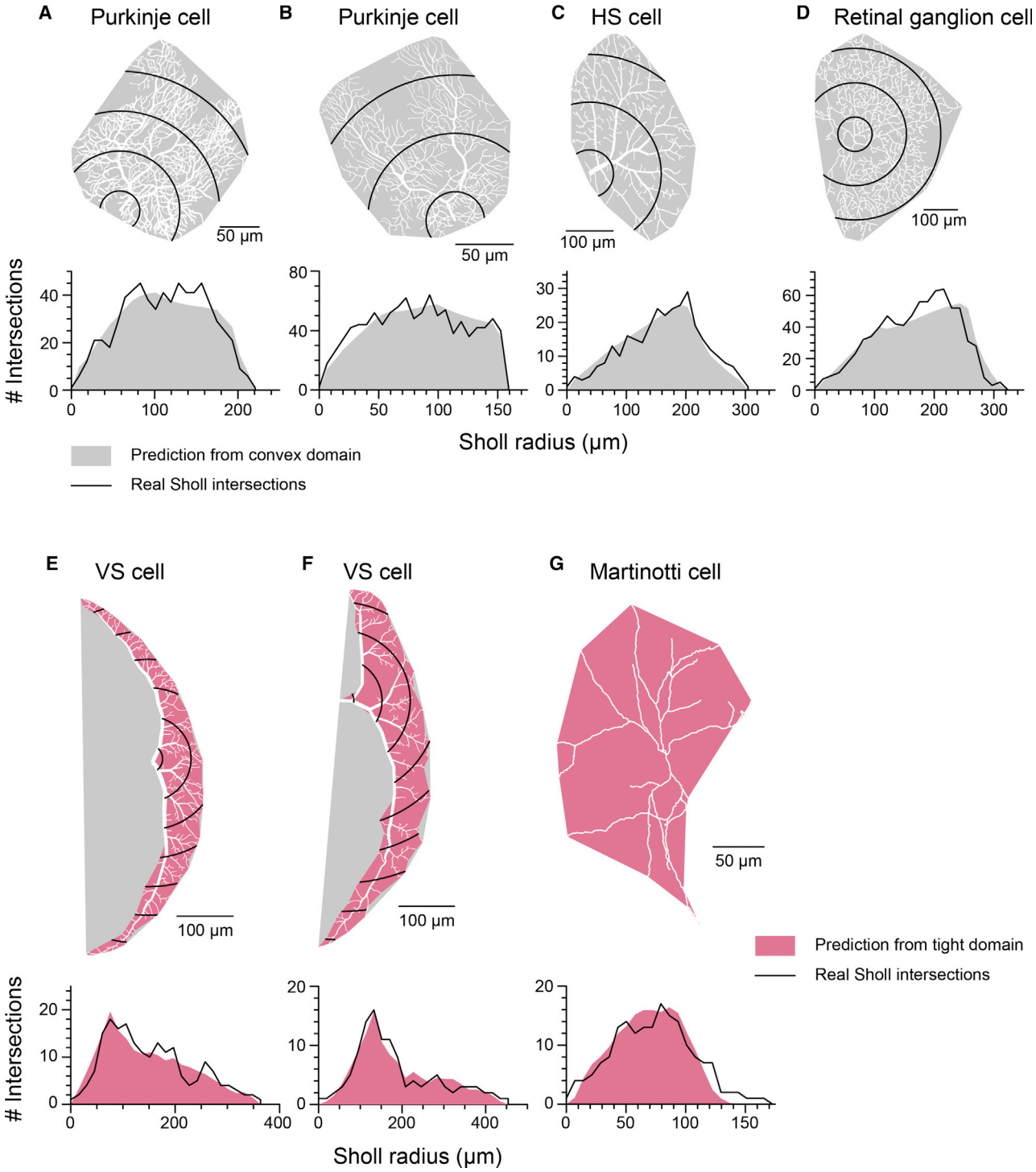

Figure 1. Sholl Intersection Profiles Estimated from Dendritic Spanning Domains

(A) Top: cerebellar Purkinje cell morphology (rat) (Vetter et al., 2001) with convex boundary (gray) and examples of circular arcs at different radii (black). Bottom: observed SIP (black) and that predicted by the domain (Equation 1, gray).

(B) Top: cerebellar Purkinje cell morphology (guinea pig) (Rapp et al., 1994). Bottom: observed SIPs (black) and domain-predicted SIPs (gray).

(C) Top: tangential HS cell morphology (blowfly) (Cuntz et al., 2008). Bottom: observed SIPs (black) and domain-predicted SIPs (gray).

(D) Top: retinal local projecting ganglion cell morphology (rabbit) (Guo et al., 2013). Bottom: observed SIPs (black) and domain-predicted SIPs (gray).

(legend continued on next page)

incorporated easily into the SIP prediction with Equation 2, this does not appear to have a large effect on the SIP of most cells.

A more common deviation from the domain-based prediction arises when dendritic branches are distributed non-isotropically and are more or less likely than chance to point toward the soma. A neuron with the majority of dendritic branches pointing toward the soma has a centripetal bias. Centripetal bias arises as dendrites connect synapses to the soma and must balance minimizing the metabolic costs associated with large lengths of dendritic cable with the delays introduced when synaptic currents must travel longer distances to reach the soma (Cuntz et al., 2007; Wen and Chklovskii, 2008). Different classes of neurons typically strike different balances between these two costs (Cuntz et al., 2010), but intuitively a neuron that prioritizes minimal conduction delays over total dendritic length will have a stronger centripetal bias, because branches pointing directly toward the soma provide the most direct path for synaptic currents. Centripetal bias results in a distribution of dendritic cable with a proximal shift compared to that predicted by a domain-based SIP. This can be seen in dentate gyrus granule cells (Figure 2C), in which dendritic branches point preferentially toward the soma and the measured SIP is more proximal than that given by Equation 1.

The biases caused by these two sources of error can be estimated by comparing the mean value $\mu_s = \int_0^R rs(r)dr$ of the true (normalized) SIP with that of the domain-based estimate μ_{s_d}. Figure 2C plots the distribution of differences in mean $\mu_s - \mu_{s_d}$ between observed and estimated SIPs for cells of different classes. The bias caused by a pure radial shift in density for the starburst amacrine cells causes a typical shift of around 10μm, or around 5% of the typical maximum radius R, whereas the other planar cell classes have smaller shifts. For three-dimensional cells, the dentate gyrus granule cells have a larger shift of around 40μm, or well over 10% of the typical maximum radius R, whereas the layer V Martinotti cells do not have a large shift in mean. Moreover, this shift can be seen in other three-dimensional cell classes and is more typical than the unbiased domain-based estimate achievable for Martinotti cells.

The following sections discuss measuring centripetal bias, its relation to the scale of the SIP, and incorporating it into the final prediction.

The Root Angle: Introducing a Direct Measure of Centripetal Bias

Existing dendritic metrics (Lorente de Nò, 1934; Bok, 1936; Ascoli et al., 2007) do not explicitly measure centripetal bias. Although there is some correlation between centripetal bias and measures such as the mean branch angle and the ratio of mean path length to total dendritic length, a direct measurement is necessary to quantitatively describe this phenomenon. The root angle θ_r is defined as the angle between a dendritic segment (defined centripetally from the termination point to the soma) $\bar{\mathbf{d}}$ and the direct path to the soma $\bar{\mathbf{r}}$ (Figure 3A):

$$\theta_r = \cos^{-1}\left(\frac{\bar{\mathbf{d}}\cdot\bar{\mathbf{r}}}{|\bar{\mathbf{d}}|\,|\bar{\mathbf{r}}|}\right) \qquad \text{(Equation 3)}$$

This can be computed at all points over a dendrite to give a distribution $f_r(\theta_r)$ of root angles (Figure 3B).

The root angle distribution of a dendrite is a direct measure of the centripetal bias and depends on both the branching properties of the dendrite and the shape of the dendrite spanning domain. In the dendritic tree structures that we studied, the root angle distribution could often be matched to a modified von Mises distribution (see STAR Methods). The von Mises distribution is the maximum entropy distribution for angles with a known directional bias, in this case toward the soma (Forbes et al., 2011). It depends on a single parameter κ, which controls the strength of the centripetal bias; when $\kappa = 0$, there is no bias and root angles are distributed uniformly, and when $\kappa \to \infty$, all dendritic segments point directly toward the soma. A larger value of κ implies that a neuron prioritizes conduction of synaptic currents over minimizing total dendritic length. Figure 3C shows our von Mises root angle model for planar and three-dimensional neurons for different values of κ. In addition, direct correspondence between the centripetal bias κ and the balancing factor *bf* (Cuntz et al., 2010) can be used to generate realistic synthetic neuronal morphologies from a generalized minimum spanning tree algorithm (see STAR Methods and Figure S3). A strong centripetal bias leads to smaller root angles, which implies that the average path length to the soma will be relatively short, corresponding to a larger balancing factor.

The von Mises model provides a good fit to most cell classes (see also Table S1), with horizontal system (HS) and VS cells the notable exceptions among the planar cells. The root angle distribution of the HS cells has a relatively linear decrease, with θ_r for root angles less than around $\pi/2$, and a shallower decline compared to the von Mises model in this region, followed by a steep drop for larger root angles. This implies that HS cells are relatively less likely to have dendritic segments pointing away (at an angle greater than $\pi/2$) from the soma than is typical for otherwise similar cell classes. Despite this difference in morphology, the domain-based SIP estimate is a good fit to the observed profiles (Figure 1C). The VS cells have a peak at non-zero θ_r, which arises from the particularly non-convex domain spanned by these cells (Figures 1E, 1F, and S2E): the root angles converge to a point distinct from the soma.

A useful visualization of the root angle distribution is to map the root angles back onto the dendritic morphology. Figure 3C

(E and F) Top: tangential VS cell morphologies type 2 (E) and type 4 (F) with convex boundary (gray) and fitted boundary (pink) (both blowfly) (Cuntz et al., 2008). Bottom: observed SIPs (black) and domain-predicted SIPs (pink).

(G) Top: cortical layer V Martinotti interneuron with fitted boundary (pink) (mouse) (Castillo-Gómez et al., 2015). Bottom: observed SIPs (black) and domain-predicted SIPs (pink).

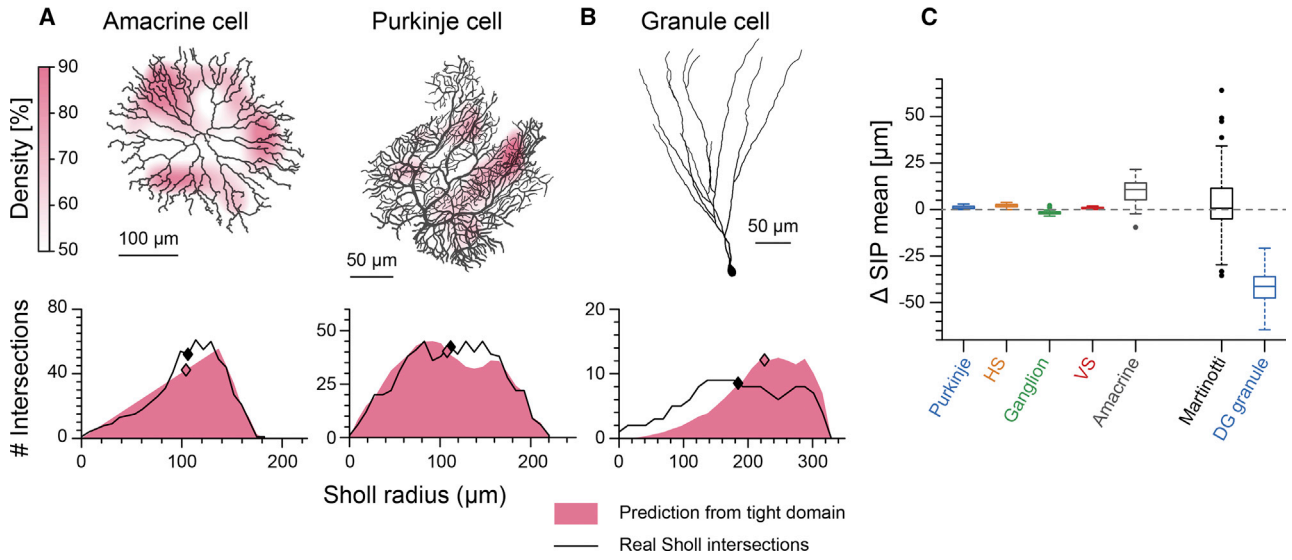

Figure 2. Limitations of the Dendrite Spanning Field

(A) Top left: retinal starburst amacrine cell morphology (rabbit) (Bloomfield and Miller, 1986) with the density of the dendritic cable shown by heatmap. Bottom left: observed SIPs (black) and domain-predicted SIPs (pink), with mean values indicated by diamonds of the appropriate color. Top right: cerebellar Purkinje cell morphology (rat) (Vetter et al., 2001) with the density of the dendritic cable shown. Bottom right: observed SIPs (black) and domain-predicted SIPs (pink), with mean values indicated by diamonds of the appropriate color.

(B) Top: hippocampal dentate gyrus granule cell (rat) (Beining et al., 2017a). Bottom: observed SIPs (black) and domain-predicted SIPs (pink), with mean values indicated by diamonds of the appropriate color.

(C) Distribution of differences in observed and estimated SIP means. Positive values indicate that the observed mean is more distal than the estimated mean, and negative values indicate the converse. Distributions are over the numbers of cells given in Table S1, with 17 starburst amacrine cell morphologies.

shows this for various cell classes, highlighting the relatively broad distributions of root angles for planar Purkinje and HS cells compared to the three-dimensional granule and CA1 pyramidal cells. Root angle distributions are consistent among different cells of the same class. Figure 3C also plots the distributions taken over all morphologies of each cell class in this paper as a solid line and the 50% and 75% ranges taken by the root angle distributions of individual cells within that class as shaded areas. The ranges are small compared to the differences between cell classes and allow individual cells of different types to be appropriately sorted using this measure.

Assuming a von Mises fit to the root angle distribution allows accurate inference on κ from relatively few samples, each requiring only a short dendritic segment, for planar (around 10) and three-dimensional (around 100) neurons (see Appendix 1 and Figure S4). This makes the root angle distribution valuable even when incomplete neuronal reconstructions are available.

Scale of the SIP

So far we have shown that the domain-based SIP (Equation 1) is approximately proportional to the measured SIP for classes of neuron that do not exhibit a strong centripetal bias. To obtain the scale of the measured SIP, it has been necessary to multiply the normalized prediction by the integral of the true SIP $A_s = \int_0^R s(r)dr$. However, there is a straightforward link between the scale and the total length of the dendritic tree: for all observed classes of neuron, there is a strong linear relationship between the scale and the total dendritic length L_d (Figure 4A):

$$A_s \propto L_d \qquad \text{(Equation 4)}$$

This relationship arises from each dendritic segment having some radial component that increases the magnitude of the SIP. This component is given by the cosine of the root angle θ_r, so the proportionality can be written as follows:

$$A_s = L_d \left[\int_0^{\pi} |\cos(\theta_r)|\, f_r(\theta_r) d\theta_r \right]^{-1} \qquad \text{(Equation 5)}$$

L_d provides a robust measure of overall dendritic size (Brown et al., 2008) and has known general relationships to the size of the spanning domain (Teeter and Stevens, 2011) and expected synaptic density (Cuntz et al., 2012). Although both the fractal dimension (Caserta et al., 1995; Fernández and Jelinek, 2001) and several Sholl-derived statistics (Rajković et al., 2016) have been shown to possess additional explanatory power for the total dendritic length, this is the first time that the simple relationship between SIP integral and L_d has been precisely quantified.

Given the analytical forms of $f_{r,2}$ and $f_{r,3}$, the von Mises models of the root angle distribution in two and three dimensions (see STAR Methods and Equations 8 and 9), it is possible to calculate the proportionality constant as a function of centripetal bias κ (Figure 4B). This prediction matches the observed values for most cell classes, with exceptions for the HS cells (orange)

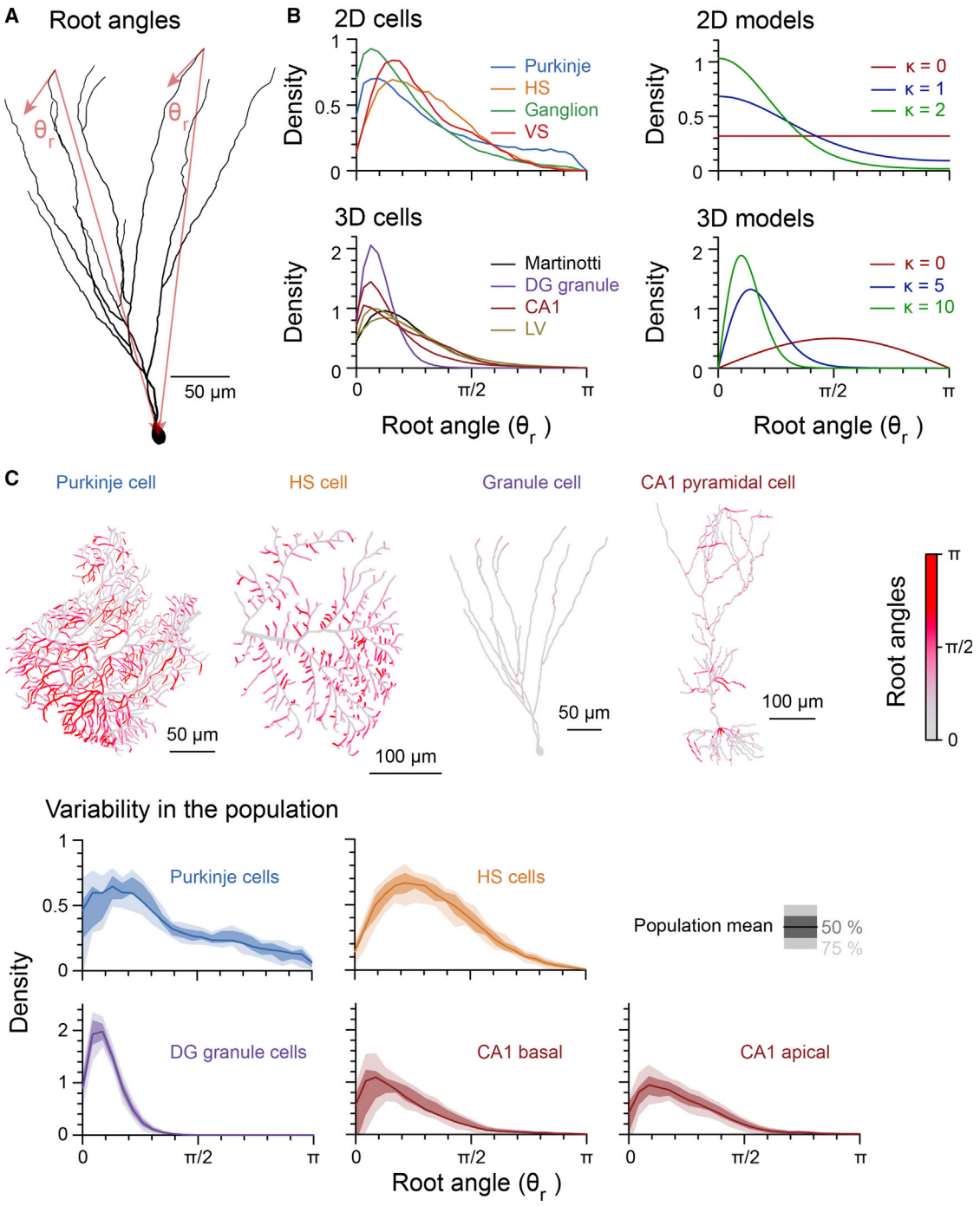

Figure 3. The Root Angle

(A) Schematic of the root angle calculation (red vectors) on dentate gyrus granule cell morphology (mouse) (Beining et al., 2017a).

(B) Left: distribution of root angles for planar neuronal classes (top) and three-dimensional neuronal classes (bottom). The number of cells in each class is given in Table S1. Right: analytical root angle distributions for planar neurons (top, Equation 8) and three-dimensional neurons (bottom, Equation 9) for different centripetal biases κ.

(C) Top: root angles projected onto neurons in two and three dimensions. Cerebellar Purkinje cell (rat) (Vetter et al., 2001), HS cell (blowfly) (Cuntz et al., 2008), dentate gyrus granule cell (rat) (Beining et al., 2017a), and hippocampal CA1 pyramidal cell (rat) (Marcelin et al., 2012). Dendritic radii are increased by 1 µm to highlight the root angles. Bottom: variation in root angle distributions for the cell classes shown above. Solid lines show the distribution over the entire cell class, the darker shaded areas show the interquartile range over all individual distributions, and the lighter shaded areas show the 75% range.

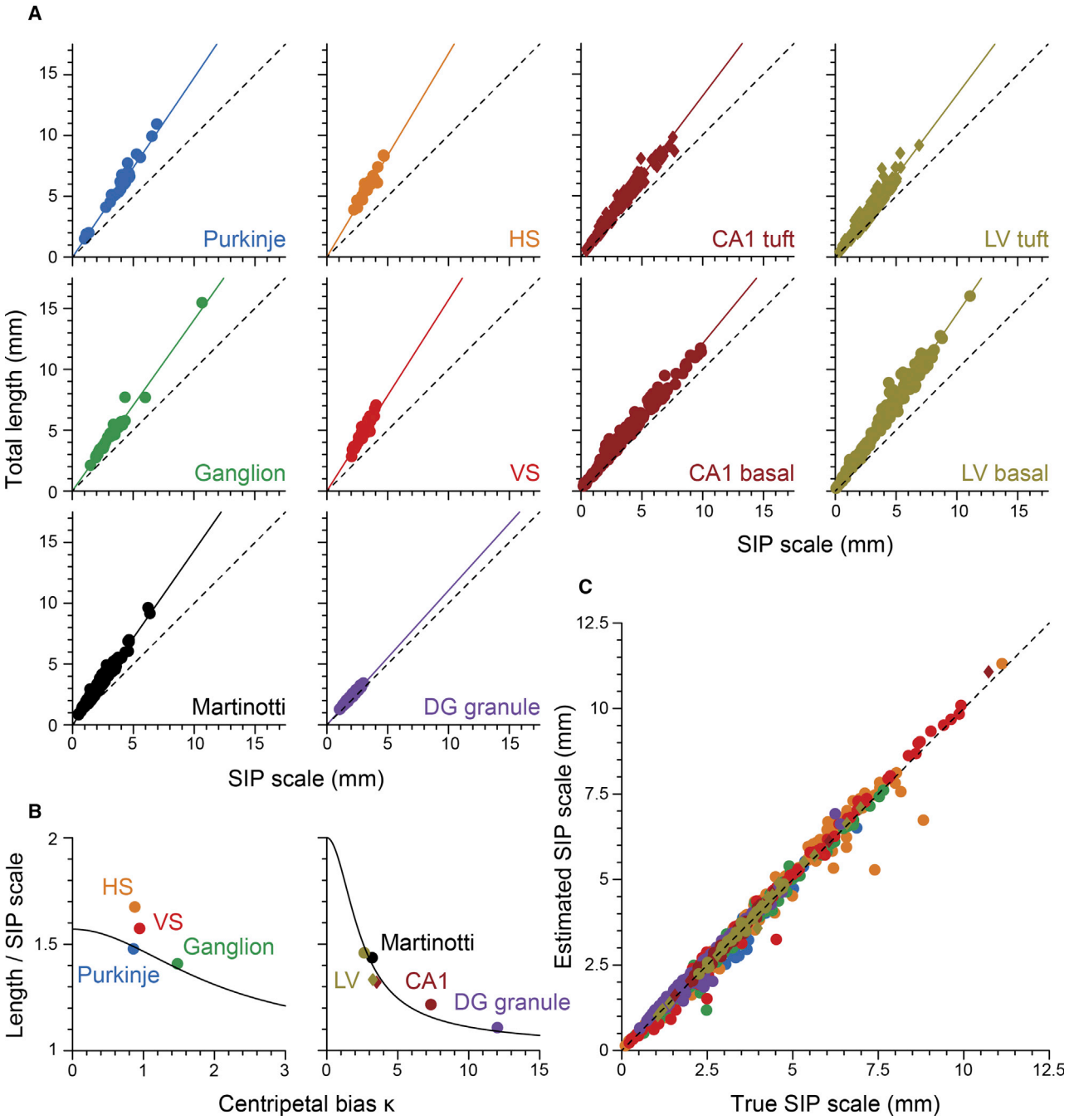

Figure 4. Scale of the SIP

(A) Total dendritic length L_d as a function of the scale of SIP A_s for different cell classes as labeled. For pyramidal cells, basal dendrites are given by circles and apical tuft dendrites are given by diamonds of the appropriate color. The number of cells in each class is given in Table S1. Linear fits (solid black lines) to the scatterplots have the following proportionality constants: Purkinje, 1.47; retinal ganglion, 1.67; HS tangential, 1.41; VS tangential, 1.57; layer V Martinotti, 1.43; dentate gyrus granule, 1.10; CA1 pyramidal basal, 1.21; CA1 pyramidal apical (diamonds), 1.32; layer V pyramidal basal, 1.46; and layer V pyramidal apical (diamonds), 1.33. Equality is shown by the dashed black line in each case.

(B) Proportionality constant as a function of centripetal bias κ for planar neurons (left) and three-dimensional neurons (right). For pyramidal cells, basal dendrites are given by circles and apical dendrites are given by diamonds. Fits (black lines) are from Equation 5.

(C) Predicted SIP scale against true SIP scale A_s for each cell. The black line shows equality.

and VS cells (light red), which have root angle distributions relatively poorly described by the von Mises model (as explained earlier). In these cases, using the exact empirical root angle distributions in Equation 5 provides a better match; at the level of individual cells, there is a tight correspondence between the estimate provided by Equation 5 and the observed ratio between total dendritic length L_d and SIP integral A_s (Figure 4C).

The proportional relationship between total dendritic length L_d and SIP integral A_s, with the proportionality following directly from the root angle distribution, allows estimated proportional SIPs to be scaled up to match the size of the dendrite and provides another functional component necessary to accurately predict observed SIPs.

Sholl Analysis Predicted by Domain, Dendritic Length, and Centripetal Bias

Given the root angle distribution $f_r(\theta_r)$, the domain $\mathbb{D}$, and the total dendritic length L_d, it is possible to obtain a better estimate of the true SIP when a neuron has a strong centripetal bias. The effect of a strongly biased root angle distribution means that dendritic segments originating outside a Sholl radius r under consideration are more likely than usual to cross it (Figure 5A), effectively shifting the mass of the SIP to the left (centripetally). The second approximation $s_r(r)$ to the SIP is therefore given by convolving the domain-based approximation $s_d(r)$ (Equation 1) with the mass of the root angle distribution at a given angle

$$s_r(r) = \int_0^R s_d(r)\phi(r-\tau)d\tau, \qquad \text{(Equation 6)}$$

where $\phi(x)$ is the density of the root angle distribution as a function of radial distance x scaled by the estimated mean branch length (see STAR Methods). This form can give a closer approximation to the true SIP $s(r)$ in cases in which the root angle distribution is relatively steep (Figure 5B, red lines).

Incorporating the root angle distribution in the form of the preceding convolution gives a centripetal shift in the SIP and allows estimation of a function s_r proportional to the true intersection profile for most neurons. Two types of pyramidal cell are introduced as examples: the cortical layer V cell and the hippocampal CA1 cell (Figure 5B). For these cells, it is common to consider the basal dendrites and the apical tuft dendrites as separate compartments, with a second center of the SIP at the top of the apical trunk (Sholl, 1953; Johnson et al., 2016; Keil et al., 2017). The implementation of this compartmentalization is discussed in STAR Methods and shown in Figure S5. The root angle-based SIP provides an accurate fit to both the basal and the apical tuft dendrites (Figure 5B). Combining the proportional form (Equation 6) with the scale given by the total dendritic length and centripetal bias (Equation 5) provides an accurate estimate of the SIP for most cell classes.

A MATLAB Trees Toolbox function *dissectSholl _tree* to estimate the SIP using this method is published in Methods S1.

Predicting Sholl-Based Metrics

Alongside the SIP, several Sholl-based metrics have been developed to enable quantitative comparison of different SIPs. The ability of the prediction method to reproduce such values provides an important addition to the functional interpretation of Sholl analysis and shows how well the dissected SIP estimates the true intersection profile for large numbers of reconstructed cells. We focus on several metrics that are commonly used to analyze SIPs: the center of mass, which defines the mean radial distance of the dendritic branches; the critical value and dendrite maximum, which quantify the location and the maximum extent of the dendrite; the regression coefficients, which describe the increasing complexity of the dendrite with distance; and the branching index, which provides an alternative measure of increasing complexity. See STAR Methods for a detailed description of each metric.

Figure 5C shows the relationship between observed and estimated (from Equations 5 and 6) Sholl-based metrics for 1,187 neuronal morphologies from the eight cell classes discussed so far. There is typically good agreement between the two values, particularly for the more direct measures of center of mass, critical value, and dendrite maximum. There is a wider dispersion of the regression coefficients, because these are known to be sensitive to small differences in morphology close to the soma (Caserta et al., 1995). A well-known metric that cannot be fitted directly is the Schoenen ramification index (Schoenen, 1982), which divides the dendrite maximum by the number of distinct dendritic branches connected to the soma. Because the estimated SIP does not typically provide a reliable value for the latter quantity, it might be necessary to consider a direct count of such branches alongside the accurate estimate of the dendrite maximum. The branching index, introduced by Garcia-Segura and Perez-Marquez (2014), provides an alternate metric for ramification that is predictable from the SIP and has been shown to be a more specific metric than the Schoenen ramification index.

Interpreting Changes in SIP

The SIP is widely used to analyze differences and changes in dendritic morphologies (see, for example, Rekha et al., 2011; Williams et al., 2013; Peng et al., 2015; Johnson et al., 2016; Chittajallu et al., 2017; Keil et al., 2017). We have shown previously that the SIP can be accurately predicted from three factors with more functional interpretations: the dendrite spanning field, the centripetal bias, and the total length. In Appendix 2 and Figure S6, we show how changing each of these three factors directly changes the shape of the SIP in a toy model (Equations 15 and 16). Given an SIP, we can say that in general a larger maximum extent implies a larger region in which synaptic contacts can be received; peaks and troughs in the SIP can imply regions where synapses are more or less likely to form; a greater scale implies a longer, denser dendritic tree potentially receiving a greater average concentration of axonal inputs; and a stronger centripetal bias, indicated by more proximal Sholl intersections than predicted by the domain, implies a neuron that prioritizes fast and efficient propagation of synaptic currents over the constraints of pure minimal wiring. There is necessarily degeneracy in describing a two- or three-dimensional dendrites by a one-dimensional

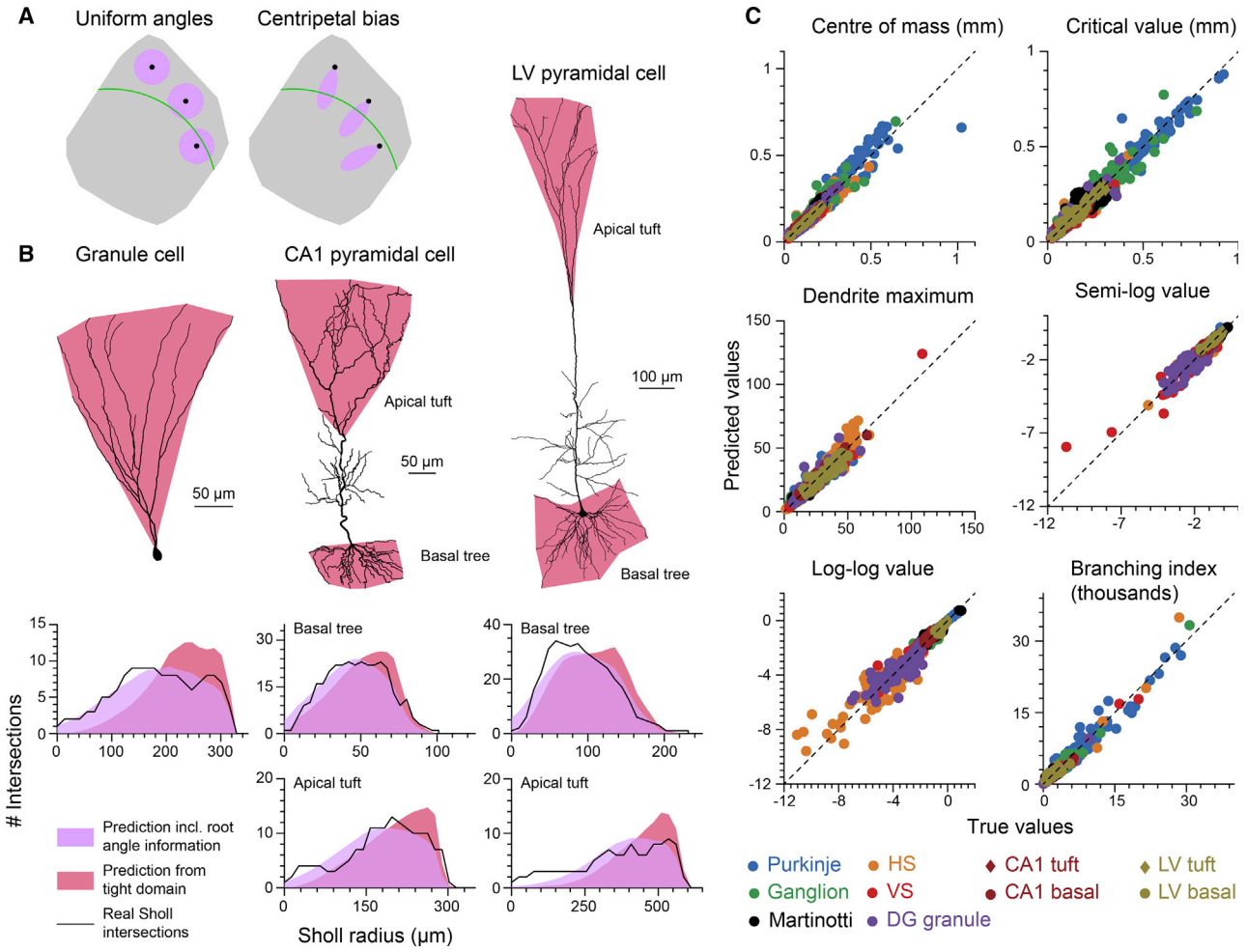

Figure 5. Sholl Analysis Predicted by Domain and Centripetal Bias

(A) Schematic showing the effect of centripetal bias on SIP calculation. The convex boundary of a Purkinje cell (rat) (Vetter et al., 2001) is shown (gray) with a Sholl radius (green). Left: a uniform root angle distribution, in which the sample points (black) are equally likely to be connected in any direction and thus influence a circular region (pink). Right: a centripetally biased root angle distribution, in which the sample points (black) preferentially connect toward the soma and thus influence a region (pink) more proximal than distal.

(B) Top left: dentate gyrus granule cell (rat) (Beining et al., 2017a), with the tight domain shaded in pink. Bottom left: observed SIPs (black), domain-based SIPs (Equation 1, pink), and root angle-based SIPs (Equation 6, purple). Top center: hippocampal CA1 pyramidal cell (rat) (Marcelin et al., 2012), with the tight domain around apical tuft and basal regions shaded in pink. Bottom center: observed SIPs (black), domain-based SIPs (Equation 1, pink), and root angle-based SIPs (Equation 6, purple) in the basal regions (above) and apical tuft regions (below). Top right: cortical layer V pyramidal cell (rat) (Hay et al., 2011), with the tight domain around apical tuft and basal regions shaded in pink. Bottom right: observed SIPs (black), domain-based SIPs (Equation 1, pink), and root angle-based SIPs (Equation 6, purple) in the basal regions (above) and apical tuft regions (below).

(C) Comparison of measured (horizontal axis) and estimated (vertical axis) Sholl-based metrics (see STAR Methods). The number of cells in each class is given in Table S1. The black dashed line in each case shows equality between measured and estimated metrics.

SIP (i.e., two different neurons could have an identical SIP), but the three functional components described here allow better consideration of how different roles could lead to a similar SIP; a proximal peak in the SIP could result from an abundance of terminating short dendritic branches or a relatively strong centripetal bias, and considering the root angle distribution would allow these two cases to be distinguished. Here, we consider three studies into differences and changes in real neuronal morphologies and discuss the insights that can be drawn from the dissected SIP.

Scaling in Tangential HS Cells

Cuntz et al. (2013) show that the electrotonic response of the tangential HS cell is surprisingly stable between the blowfly *Calliphora vicina* and the fruit fly *Drosophila melanogaster*, despite the cell of the latter being around four times smaller in each dimension (Figure 6A, top). The SIPs (Figure 6A, center) of the two sets of cells reveal a similar form due to the similar dendrite spanning domains, with the *Drosophila* cells having greater density. Despite the average spanning domain being 10.1 times larger in the *Calliphora* cells, the SIP scale A_s is only

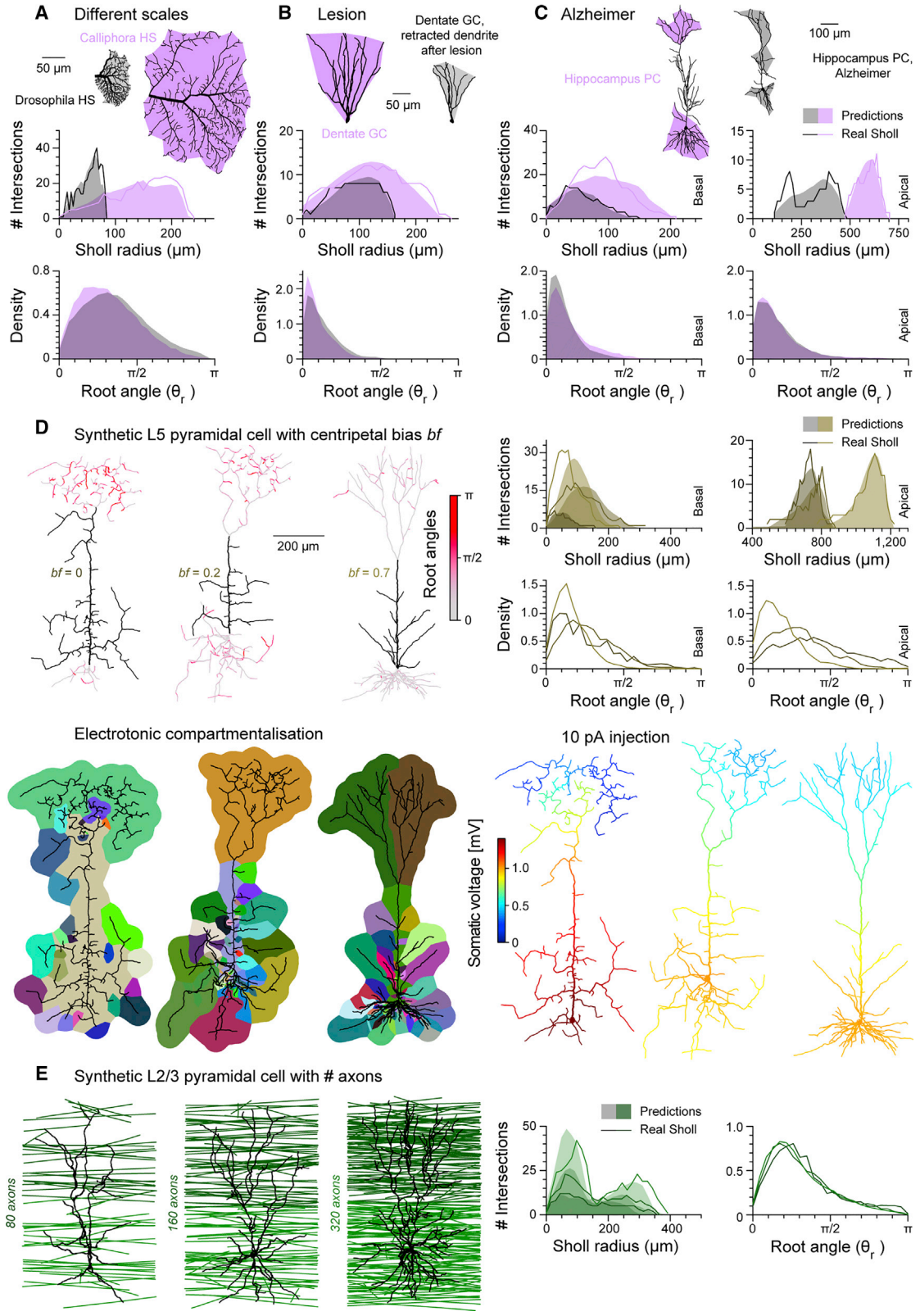

(legend on next page)

1.42 times larger. The fitted centripetal bias κ (Figure 6A, bottom) changes from 0.66 in the *Calliphora* case to 0.47 for the *Drosophila* case, but there is substantial overlap in their confidence intervals and this result is not significant at the 10% level. This observation supports the more detailed morphometric analysis in that paper.

Dendritic Retraction in Lesioned Granule Cells

Vuksic et al. (2011) studied the sustained effects on the morphology of dentate gyrus granule cells of lesioning the axonal input. Figure 6B (top) plots examples of pre- and post-lesioned granule cells. The resultant change in SIP between the two cases (Figure 6B, center) shows no difference in the proximal region and a sharper fall more distally. This corresponds to a change in the dendrite spanning domain in response to the lack of innervation, with no difference in dendritic density and little change in centripetal bias (Figure 6B, bottom).

Alzheimer's in Hippocampal CA1 Pyramidal Cells

Šišková et al. (2014) link degradation of the dendritic structure to functional hyperexcitability in hippocampal CA1 pyramidal neurons (Figure 6C, top) in a mouse model of Alzheimer's disease. The SIPs of both the basal and the apical tuft show reductions in both density and spanning area (Figure 6C, center). There is almost no change in the root angle distribution in the apical tuft and a slight increase in centripetal bias in the basal dendrites (Figure 6C, bottom): the wild-type CA1 cells have a κ value of 9.09 (7.90 to 10.28) and the Alzheimer's cells have a κ value of 12.75 (11.49 to 14.01), giving a one-sided p value of 0.051. The mouse model of Alzheimer's in hippocampal CA1 cells displays changes in each of the three factors that predict the SIP.

Changes in Centripetal Bias for Cortical Layer V Pyramidal Cells

The centripetal bias shown by the root angle distribution is closely related to the generative balancing factor *bf* (Figure S3) used to produce synthetic neuronal morphologies with a generalized minimum spanning tree (Cuntz et al., 2010). It is therefore possible to investigate the effects of an altered centripetal bias on the morphology, SIP, and root angle distribution of a particular cell class. Cuntz et al. (2010) introduced an example model of a cortical layer V pyramidal cell with a physiologically realistic balancing factor of 0.7 and two lower values, 0.2 and 0. Taking these morphologies (Figure 6D, upper left-hand side) and analyzing the root angle distributions and SIPs illustrates how the dissected Sholl profile captures the changes in a neuron's morphology. The root angle distributions (Figure 6D, upper right-hand side, top) in both the basal and the apical regions show a large difference in centripetal bias between the realistic morphology and the two cases that prioritize wiring length over conduction delays. The SIP (Figure 6D, upper right-hand side, bottom) similarly show a marked difference between the morphologies, although here the effect of changing centripetal bias is confounded by differences in the spanning domain and total dendritic length (as shown by Equation 5).

The effect of different centripetal biases on the functionality of the neuron is shown by considering the electrotonic compartmentalization and current transfer properties of the neurons. An electrotonic compartment of a neuron is defined in Cuntz et al. (2010) as a region within which the attenuation of current remains below a certain level, the compartmentalization is the set of all such compartments. It has previously been noted that a higher value of *bf* and therefore a higher centripetal bias typically leads to more electrotonic compartments, because synaptic currents have more direct paths to the soma and are relatively isolated from inputs to neighboring branches. This effect is maintained here (Figure 6D, lower left-hand side), where the pyramidal cells with weaker centripetal biases have relatively few (29 and 36 compartments) electrotonic compartments compared to the realistic model (52 compartments). Directly calculating the voltage change at the soma due to synaptic currents at different sites, referred to as the transfer resistance, reveals a similar picture (Figure 6D, lower right-hand side). The left-hand cell with minimal centripetal bias has a relatively short dendritic

Figure 6. Interpreting Changes in SIP

(A) Top: HS visual cells from the fruit fly *Drosophila* (left, gray shading) and blowfly *Calliphora* (right, purple shading) (both from Cuntz et al., 2013). Center: comparison of measured SIPs (solid lines) and predicted SIPs (shaded areas) for the fruit fly *Drosophila* (gray, 20 cells) and blowfly *Calliphora* (purple, 25 cells). Bottom: Comparison of the root angle distributions for the fruit fly *Drosophila* cells (gray) and blowfly *Calliphora* cells (purple).

(B) Top: dentate gyrus granule cells before (left, purple shading) and after (right, gray shading) perforant path lesion, causing denervation of the distal dendrites (both mouse) (Vuksic et al., 2011). Center: comparison of measured SIPs (solid lines) and predicted SIPs (shaded areas) without lesion (purple, 15 cells) and with lesion (red, 15 cells). Bottom: comparison of the root angle distributions without lesion (purple) and with lesion (gray).

(C) Top: hippocampal CA1 pyramidal cells, wild-type (left, shaded purple) and in a transgenic model of Alzheimer's (right, shaded gray) (both mouse from Šišková et al., 2014). Center: comparison of measured SIPs (solid lines) and predicted SIPs (shaded areas) for wild-type (purple, 23 cells) and Alzheimer's model (gray, 22 cells) in the basal regions (left) and apical tuft regions (right). Bottom: comparison of the root angle distributions in the wild-type cells (purple) and Alzheimer's model cells (gray) in the basal regions (left) and apical tuft regions (right).

(D) Upper left: synthetic layer V cortical pyramidal cells generated with different balancing factors: $bf = 0$, 0.2, 0.7 from left to right. Morphologies originally generated by Cuntz et al. (2010). Root angles are projected onto the morphologies in the basal and apical tuft regions. Upper right, top: SIPs for the basal compartments (left) and apical compartments (right) for the three morphologies. Measured SIPs are given by solid lines, and those predicted by the domain and root angle distribution are given by shaded areas. Upper right, bottom: root angle distributions in the basal compartments (left) and apical compartments (right) for the three morphologies. Lower left: electrotonic compartmentalization of the above cells. Compartments are defined by the region within which current attenuation remains below 86%, and colors are randomly assigned to compartments. Passive electrotonic properties are axial resistivity of 100 Ωcm and membrane conductivity of 5×10^{-5} s/cm^2. Lower right: transfer resistance to the soma with the above passive electrotonic parameters. Dendritic radii are increased by 1 μm in the figure to aid visualization.

(E) Left: synthetic layer II/III cortical pyramidal cells for different axonal densities generated using the model defined in Cuntz (2012). The number of axons (green lines) increases from left to right. Right: SIPs and root angle distributions for the three morphologies. Measured SIPs are given by solid lines, and those predicted by the domain and root angle distribution are given by shaded areas.

tree and thus has a high transfer resistance for synaptic sites close to the soma, because currents cannot readily disperse into dendritic branches (Rall, 1957). Further from the soma, however, the transfer resistance drops dramatically and distal synaptic inputs have a negligible impact on somatic voltage. For a pyramidal cell with realistic centripetal bias, the range of transfer resistances is narrower, and in particular, synaptic inputs at similar physical distances from the soma have a similar influence.

Changes in Axonal Density for Cortical Layer II/III Pyramidal Cells

Cuntz (2012) and Mazzoni et al. (2015) considered models of various neuronal morphologies using the distribution of proposed axonal inputs to inform possible synaptic locations. This approach enables us to demonstrate how the SIP, and in particular its scale, relates to the density of axons synapsing onto a dendrite. Figure 6E shows the effect on synthetic cortical layer II/III pyramidal cell morphologies of increasing (from left to right) the number of axons (shown in green) passing through its spanning field without altering the centripetal bias. Considering the SIPs of the respective cells, the main difference is the scale. The integral of the SIP increases from 2,233 to 3,921 and then to 7,063 μm, reflecting total dendritic lengths of 3,306, 5,543, and 10,069 μm, respectively. The root angle distributions are not substantially altered by the changes in axonal density, showing little change in centripetal bias. This means that the ratio of total dendritic length to SIP scale remains around 0.7 in all cases (specifically, 0.68, 0.71, and 0.70, respectively). The relationship between density of synaptic targets and dendrite length has previously been studied by Cuntz et al. (2012) and appears to follow a power law; here we provide a description of how the density of axonal inputs appears in the SIP through the effect on dendritic length.

DISCUSSION

We have shown that the SIP of a neuron can be accurately predicted from three basic measures with known functional interpretations. These are the domain spanned by the dendrite, in which it can receive synaptic connections; the total length of the dendrite within this domain, which defines the average density; and the centripetal bias, which depends on the balance between conduction delays and total dendritic cost. The centripetal bias is quantified by a measure called the root angle distribution, which is a widely applicable metric of dendritic morphology. The approximation from these three basic features is accurate for various cell classes from various species.

We have found that for many classes of neuron, the relative size of the domain spanned by the dendrite at a given distance is proportional to the SIP. This result relies on the self-similarity (Wen et al., 2009; Snider et al., 2010) and surprising relative uniformity of dendritic trees within their respective bounds and means that the shape of an SIP can often be taken as a proxy for connectivity and microcircuit structure, because it relies strongly on the area reached by the dendrites, where intersecting axons can make potential synapses (Stepanyants et al., 2008; Packer et al., 2013).

However, several cell classes deviate from the purely domain-based prediction, and consideration of an additional property was necessary to produce an accurate proportional estimate of the SIP. This additional factor arises from optimal wiring considerations (Cuntz et al., 2007; Wen and Chklovskii, 2008; Budd et al., 2010); neurons typically strike a balance between the total dendritic length and the mean path length from synaptic sites to the soma (Cuntz et al., 2010) and a favoring of shorter conduction times can lead to a proximal shift in dendritic mass compared to that predicted by the domain alone. To quantify this balance, we introduced a new morphometric measure: the root angle distribution. This defines the distribution of angular deviations of dendritic branches from the direct path to the soma; a cell class, which appears to prioritize minimizing total dendritic length over path length will have a broader root angle distribution than one with the opposite balance. Incorporating this factor captured the shift in dendritic mass seen in the SIP of neuronal classes that are not well explained by their domain alone.

A third factor was necessary to move from the proportional estimate discussed so far that accounts for the relative spread of dendritic complexity to the full SIP that also measures the number of dendritic branches at a given distance: the total dendritic length. The total dendritic length, combined with the domain spanned by the dendritic tree, gives the density of the dendrite with functional implications in axon abundance (Wen et al., 2009; Budd et al., 2010; Cuntz, 2012) and probability of synapse formation (Liley and Wright, 1994; Chklovskii, 2004; Packer et al., 2013). In estimating the scale, we discovered a previously unknown and strong linear relationship between the total amplitude of the SIP and the total dendritic length, with a coefficient dependent on the root angle distribution discussed earlier.

This study has several consequences for the role of Sholl analysis in both theoretical and experimental dendritic anatomy. First, the ability to predict the spatially extended SIP using two quantities, the total length and the root angle distribution, which are averaged over the entire arbor, is confirmation of the relative homogeneity of most neurons (Wen et al., 2009; Snider et al., 2010). Where particular neurons consistently deviate from the predicted SIP, as in the case of the retinal starburst amacrine cell in Figure 2, there is compelling evidence of an unusual structure that may provide insight into specific dendritic function (Famiglietti, 1991).

Second, many dendritic metrics are typically computed (Lorente de Nò, 1934; Bok, 1936; Ascoli et al., 2007) to allow classification into cell classes (DeFelipe et al., 2013) or produce realistic synthetic cells for modeling studies (Koene et al., 2009; Cuntz et al., 2010). That the SIP is so insensitive to most of these metrics means that it may often be possible to substantially simplify the dendritic structures under consideration. The three factors that predict the SIP determine the location, average density, and orientation of dendritic branches; potentially greatly reducing the number of factors necessary to model features such as synaptic locations. One of the earliest theoretical predictions of synaptic formation probability in Liley and Wright (1994) relied on the analytical simplifications available from the SIP, before similar methods could be applied using more data and computational power to determine precise axon-dendrite appositions (Hill et al., 2012). The dissected SIP, by focusing on the

essential factors in dendritic placement, has the potential to offer new insights into the connectivity of neuronal networks and how connectivity depends on the features of the constituent cell classes.

It is typically simpler and less labor intensive to record an SIP from a recorded image stack, using software such as that in Kutzing et al. (2010) or Ferreira et al. (2014), than to produce a full three-dimensional reconstruction (Donohue and Ascoli, 2011; Radojević and Meijering, 2017). With increases in the usage of relatively high-throughput imaging techniques (Wu et al., 2004; Gong et al., 2016), Sholl analysis is a valuable technique to evaluate such data. By defining the functional aspects of a dendrite that give rise to a particular SIP, this study makes it possible to better interpret measured SIPs. The total dendritic length and the dendrite spanning field are both relatively easy to recover from noisy images, and the root angle distribution can typically be inferred from a limited number of samples (see Appendix 1). That it is also possible to accurately estimate total dendritic length from the SIP and root angle distribution is a major finding. The ability to record the key features from large numbers of cells has broad experimental applications. For example, changes in dendritic structure are widely related to neuronal pathologies, ranging from autism spectrum disorder to fragile X syndrome (Kulkarni and Firestein, 2012). Many characteristics of these diseases are most apparent on a small scale, such as abnormalities in dendritic spines, while larger-scale changes are poorly understood (Copf, 2016) but still apparent in the Sholl profile (Williams et al., 2013; Šišková et al., 2014). Widespread imaging of healthy and pathological neurons and functional understanding provided by these measures could provide new understanding the effects of such conditions on a neuronal scale.

The Root Angle

The root angle distribution provides a metric for dendritic arborization with applications distinct from its use in estimating the SIP. The root angle distribution gives a direct and unambiguous measure of centripetal bias for an observed tree, allowing the generative balancing factor used in generalized minimum spanning tree construction to be inferred simply, rather than fitted to several other metrics (Cuntz et al., 2007, 2010). The root angle distribution therefore has the potential to reveal important differences in neuronal growth processes. The root angle distribution depends on the spanning field, but this dependence is weak for most actual neurons and crucially provides extra information about neuronal structure. The most effective morphological classification techniques to date rely on the dendritic density field in context (Sümbül et al., 2014; Jiang et al., 2015) or related topological measures (Kanari et al., 2018). Adding the root angle may substantially improve the performance of such techniques and increase the accuracy of neuronal classification.

Extensions

An interesting extension to our work could come from incorporating knowledge of the dendritic diameter to allow for a representation of the amount of dendrite at a given electrotonic distance from the soma. The diameter can be either measured experimentally or estimated from the typical tapering behavior of dendrites (Cuntz et al., 2007; Bird and Cuntz, 2016). Such a technique has been used to understand the effects of backpropagation in different dendritic morphologies (Vetter et al., 2001), and wider application could greatly simplify cable-theory modeling in realistic dendrites. The development of the T2N tool (Beining et al., 2017b), which links straightforward morphological modeling under the MATLAB Trees Toolbox package (Cuntz et al., 2010) with detailed electrophysiological simulations using NEURON (Hines and Carnevale, 1997), also enables study of the relationships among the SIP, its functional components, and active dendritic processes. Sholl analysis has also been applied to axonal arborizations, particularly in the spinal cord (Kigerl et al., 2009). It would be interesting to see how far the techniques described here could be applied in that framework, particularly given the differences in structure between axons and dendrites (Budd et al., 2010; Cuntz et al., 2010). Analogues of Sholl analysis are also used outside of neuroscience, for example, to quantify cancer tumors (Stanko et al., 2015); typically, neurons obey branching statistics that are starkly different from those of other biological systems, such as arboreal trees or corals (Teeter and Stevens, 2011; Cuntz et al., 2012; Kim et al., 2012), but a similar approach to that taken in this paper may reveal the functional aspects that predict Sholl analogs in other fields.

Overall, our study provides a powerful link between the SIP, a widely used measure of dendritic complexity, and the three functional constraints that underpin it.

STAR★METHODS

Detailed methods are provided in the online version of this paper and include the following:

- KEY RESOURCES TABLE
- CONTACT FOR REAGENT AND RESOURCE SHARING
- METHOD DETAILS
  - Numerical integrals
  - Quantifying error
  - Bounding non-convex dendrites
  - Calculating root angles for reconstructed morphologies
  - Defining basal, apical trunk, and apical tuft dendrites on a pyramidal cell
  - Analytical form of root angle distribution
  - Linking root angle to balancing factor
  - The density of the root angle distribution as a function of radius
  - Sholl-based metrics
  - Electrotonics and compartmentalisation
  - Morphologies used in figures
  - Appendix 1
  - Appendix 2
- QUANTIFICATION AND STATISTICAL ANALYSIS
- DATA AND SOFTWARE AVAILABILITY

SUPPLEMENTAL INFORMATION

Supplemental Information can be found online at https://doi.org/10.1016/j.celrep.2019.04.097.

ACKNOWLEDGMENTS

We acknowledge funding through BMBF grant 01GQ1406 (Bernstein Award 2013) to H.C. Thanks to Stefan Remy, Daniel Justus, and Laura Mediavilla for providing the hippocampal CA1 morphologies used in Figure 6. Thanks to Peter Jedlicka, Lea Goetz, and Tomke Stürner for many helpful comments on the manuscript.

AUTHOR CONTRIBUTIONS

Conceptualization, A.D.B. and H.C.; Methodology, A.D.B. and H.C.; Software, A.D.B. and H.C.; Validation, A.D.B. and H.C.; Formal Analysis, A.D.B. and H.C.; Investigation, A.D.B. and H.C.; Resources, H.C.; Data Curation, A.D.B. and H.C.; Writing – Original Draft, A.D.B.; Writing – Review & Editing, A.D.B. and H.C.; Visualization, A.D.B. and H.C.; Supervision, H.C.; Project Administration, H.C.; Funding Acquisition, H.C.

DECLARATION OF INTERESTS

The authors declare no competing interests.

Received: July 5, 2018
Revised: September 20, 2018
Accepted: April 19, 2019
Published: June 4, 2019

REFERENCES

Ascoli, G.A., Donohue, D.E., and Halavi, M. (2007). NeuroMorpho.Org: a central resource for neuronal morphologies. J. Neurosci. *27*, 9247–9251.

Ascoli, G.A., Alonso-Nanclares, L., Anderson, S.A., Barrionuevo, G., Benavides-Piccione, R., Burkhalter, A., Buzsáki, G., Cauli, B., Defelipe, J., Fairén, A., et al.; Petilla Interneuron Nomenclature Group (2008). Petilla terminology: nomenclature of features of GABAergic interneurons of the cerebral cortex. Nat. Rev. Neurosci. *9*, 557–568.

Beining, M., Jungenitz, T., Radic, T., Deller, T., Cuntz, H., Jedlicka, P., and Schwarzacher, S.W. (2017a). Adult-born dentate granule cells show a critical period of dendritic reorganization and are distinct from developmentally born cells. Brain Struct. Funct. *222*, 1427–1446.

Beining, M., Mongiat, L.A., Schwarzacher, S.W., Cuntz, H., and Jedlicka, P. (2017b). T2N as a new tool for robust electrophysiological modeling demonstrated for mature and adult-born dentate granule cells. eLife *6*, e26517.

Binley, K.E., Ng, W.S., Tribble, J.R., Song, B., and Morgan, J.E. (2014). Sholl analysis: a quantitative comparison of semi-automated methods. J. Neurosci. Methods *225*, 65–70.

Bird, A.D., and Cuntz, H. (2016). Optimal current transfer in dendrites. PLoS Comput. Biol. *12*, e1004897.

Bloomfield, S.A., and Miller, R.F. (1986). A functional organization of ON and OFF pathways in the rabbit retina. J. Neurosci. *6*, 1–13.

Bok, S.T. (1936). The branching of the dendrites in the cerebral cortex. Proc. Acad. Sci. (Amst.) *39*, 1209–1218.

Brown, K.M., Gillette, T.A., and Ascoli, G.A. (2008). Quantifying neuronal size: summing up trees and splitting the branch difference. Semin. Cell Dev. Biol. *19*, 485–493.

Budd, J.M.L., Kovács, K., Ferecskó, A.S., Buzás, P., Eysel, U.T., and Kisvárday, Z.F. (2010). Neocortical axon arbors trade-off material and conduction delay conservation. PLoS Comput. Biol. *6*, e1000711.

Caserta, F., Stanley, H.E., Eldred, W.D., Daccord, G., Hausman, R.E., and Nittmann, J. (1990). Physical mechanisms underlying neurite outgrowth: A quantitative analysis of neuronal shape. Phys. Rev. Lett. *64*, 95–98.

Caserta, F., Eldred, W.D., Fernandez, E., Hausman, R.E., Stanford, L.R., Bulderev, S.V., Schwarzer, S., and Stanley, H.E. (1995). Determination of fractal dimension of physiologically characterized neurons in two and three dimensions. J. Neurosci. Methods *56*, 133–144.

Castillo-Gómez, E., Coviello, S., Perez-Rando, M., Curto, Y., Carceller, H., Salvador, A., and Nacher, J. (2015). Streptozotocin diabetic mice display depressive-like behavior and alterations in the structure, neurotransmission and plasticity of medial prefrontal cortex interneurons. Brain Res. Bull. *116*, 45–56.

Chittajallu, R., Wester, J.C., Craig, M.T., Barksdale, E., Yuan, X.Q., Akgül, G., Fang, C., Collins, D., Hunt, S., Pelkey, K.A., and McBain, C.J. (2017). Afferent specific role of NMDA receptors for the circuit integration of hippocampal neurogliaform cells. Nat. Commun. *8*, 152.

Chklovskii, D.B. (2004). Synaptic connectivity and neuronal morphology: two sides of the same coin. Neuron *43*, 609–617.

Copf, T. (2016). Impairments in dendrite morphogenesis as etiology for neurodevelopmental disorders and implications for therapeutic treatments. Neurosci. Biobehav. Rev. *68*, 946–978.

Cuntz, H. (2012). The dendritic density field of a cortical pyramidal cell. Front. Neuroanat. *6*, 2.

Cuntz, H., Borst, A., and Segev, I. (2007). Optimization principles of dendritic structure. Theor. Biol. Med. Model. *4*, 21.

Cuntz, H., Forstner, F., Haag, J., and Borst, A. (2008). The morphological identity of insect dendrites. PLoS Comput. Biol. *4*, e1000251.

Cuntz, H., Forstner, F., Borst, A., and Häusser, M. (2010). One rule to grow them all: a general theory of neuronal branching and its practical application. PLoS Comput. Biol. *6*, e1000877.

Cuntz, H., Mathy, A., and Häusser, M. (2012). A scaling law derived from optimal dendritic wiring. Proc. Natl. Acad. Sci. USA *109*, 11014–11018.

Cuntz, H., Forstner, F., Schnell, B., Ammer, G., Raghu, S.V., and Borst, A. (2013). Preserving neural function under extreme scaling. PLoS ONE *8*, e71540.

DeFelipe, J., López-Cruz, P.L., Benavides-Piccione, R., Bielza, C., Larrañaga, P., Anderson, S., Burkhalter, A., Cauli, B., Fairén, A., Feldmeyer, D., et al. (2013). New insights into the classification and nomenclature of cortical GABAergic interneurons. Nat. Rev. Neurosci. *14*, 202–216.

Donohue, D.E., and Ascoli, G.A. (2011). Automated reconstruction of neuronal morphology: an overview. Brain Res. Brain Res. Rev. *67*, 94–102.

Edelsbrunner, H., Kirkpatrick, D., and Seidel, R. (1983). On the shape of a set of points in the plane. IEEE Trans. Inform. Theor *29*, 551–559.

Famiglietti, E.V. (1991). Synaptic organization of starburst amacrine cells in rabbit retina: analysis of serial thin sections by electron microscopy and graphic reconstruction. J. Comp. Neurol. *309*, 40–70.

Fernández, E., and Jelinek, H.F. (2001). Use of fractal theory in neuroscience: methods, advantages, and potential problems. Methods *24*, 309–321.

Ferreira, T.A., Blackman, A.V., Oyrer, J., Jayabal, S., Chung, A.J., Watt, A.J., Sjöström, P.J., and van Meyel, D.J. (2014). Neuronal morphometry directly from bitmap images. Nat. Methods *11*, 982–984.

Forbes, C., Evans, M., Hastings, N., and Peacock, B. (2011). Statistical Distributions, Fourth Edition (Wiley).

Garcia-Segura, L.M., and Perez-Marquez, J. (2014). A new mathematical function to evaluate neuronal morphology using the Sholl analysis. J. Neurosci. Methods *226*, 103–109.

Gong, H., Xu, D., Yuan, J., Li, X., Guo, C., Peng, J., Li, Y., Schwarz, L.A., Li, A., Hu, B., et al. (2016). High-throughput dual-colour precision imaging for brain-wide connectome with cytoarchitectonic landmarks at the cellular level. Nat. Commun. *7*, 12142.

Guo, T., Tsai, D., Morley, J.W., Suaning, G.J., Lovell, N.H., and Dokos, S. (2013). Influence of cell morphology in a computational model of ON and OFF retinal ganglion cells. Conf. Proc. IEEE Eng. Med. Biol. Soc. *2013*, 4553–4556.

Gutierrez, H., and Davies, A.M. (2007). A fast and accurate procedure for deriving the Sholl profile in quantitative studies of neuronal morphology. J. Neurosci. Methods *163*, 24–30.

Gutthorp, P., and Lockhart, R.A. (1988). Finding the location of a signal: A Bayesian analysis. J. Am. Stat. Assoc. *83*, 322–330.

Hay, E., Hill, S., Schürmann, F., Markram, H., and Segev, I. (2011). Models of neocortical layer 5b pyramidal cells capturing a wide range of dendritic and perisomatic active properties. PLoS Comput. Biol. *7*, e1002107.

Hill, S.L., Wang, Y., Riachi, I., Schürmann, F., and Markram, H. (2012). Statistical connectivity provides a sufficient foundation for specific functional connectivity in neocortical neural microcircuits. Proc. Natl. Acad. Sci. USA *109*, E2885–E2894.

Hines, M.L., and Carnevale, N.T. (1997). The NEURON simulation environment. Neural Comput. *9*, 1179–1209.

Jiang, X., Shen, S., Cadwell, C.R., Berens, P., Sinz, F., Ecker, A.S., Patel, S., and Tolias, A.S. (2015). Principles of connectivity among morphologically defined cell types in adult neocortex. Science *350*, aac9462.

Johnson, C.B., Schall, M., Tennison, M.E., Garcia, M.E., Shea-Shumsky, N.B., Raghanti, M.A., Lewandowski, A.H., Bertelsen, M.F., Waller, L.C., Walsh, T., et al. (2016). Neocortical neuronal morphology in the Siberian Tiger (*Panthera tigris altaica*) and the clouded leopard (*Neofelis nebulosa*). J. Comp. Neurol. *524*, 3641–3665.

Kanari, L., Dłotko, P., Scolamiero, M., Levi, R., Shillcock, J., Hess, K., and Markram, H. (2018). A topological representation of branching neuronal morphologies. Neuroinformatics *16*, 3–13.

Keil, K.P., Sethi, S., Wilson, M.D., Chen, H., and Lein, P.J. (2017). *In vivo* and *in vitro* sex differences in the dendritic morphology of developing murine hippocampal and cortical neurons. Sci. Rep. *7*, 8486.

Kigerl, K.A., Gensel, J.C., Ankeny, D.P., Alexander, J.K., Donnelly, D.J., and Popovich, P.G. (2009). Identification of two distinct macrophage subsets with divergent effects causing either neurotoxicity or regeneration in the injured mouse spinal cord. J. Neurosci. *29*, 13435–13444.

Kim, Y., Sinclair, R., Chindapol, N., Kaandorp, J.A., and De Schutter, E. (2012). Geometric theory predicts bifurcations in minimal wiring cost trees in biology are flat. PLoS Comput. Biol. *8*, e1002474.

Koene, R.A., Tijms, B., van Hees, P., Postma, F., de Ridder, A., Ramakers, G.J., van Pelt, J., and van Ooyen, A. (2009). NETMORPH: a framework for the stochastic generation of large scale neuronal networks with realistic neuron morphologies. Neuroinformatics *7*, 195–210.

Kulkarni, V.A., and Firestein, B.L. (2012). The dendritic tree and brain disorders. Mol. Cell. Neurosci. *50*, 10–20.

Kutzing, M.K., Langhammer, C.G., Luo, V., Lakdawala, H., and Firestein, B.L. (2010). Automated Sholl analysis of digitized neuronal morphology at multiple scales. J. Vis. Exp. *45*, 2354.

Langhammer, C.G., Previtera, M.L., Sweet, E.S., Sran, S.S., Chen, M., and Firestein, B.L. (2010). Automated Sholl analysis of digitized neuronal morphology at multiple scales: Whole cell Sholl analysis versus Sholl analysis of arbor subregions. Cytometry A *77*, 1160–1168.

Liley, D.T.J., and Wright, J.J. (1994). Intracortical connectivity of pyramidal and stellate cells: Estimates of synaptic densities and coupling symmetry. Netw. Comput. Neural Syst. *5*, 175–189.

Lorente de Nò, R. (1934). Studies on the structure of the cerebral cortex. II. Continuation of the study of the ammonic system. J. Psychol. Neurol. *46*, 113–177.

Marcelin, B., Liu, Z., Chen, Y., Lewis, A.S., Becker, A., McClelland, S., Chetkovich, D.M., Migliore, M., Baram, T.Z., Esclapez, M., and Bernard, C. (2012). Dorsoventral differences in intrinsic properties in developing CA1 pyramidal cells. J. Neurosci. *32*, 3736–3747.

Mazzoni, A., Lindén, H., Cuntz, H., Lansner, A., Panzeri, S., and Einevoll, G.T. (2015). Computing the local field potential (LFP) from integrate-and-fire network models. PLoS Comput. Biol. *11*, e1004584.

Montague, P.R., and Friedlander, M.J. (1991). Morphogenesis and territorial coverage by isolated mammalian retinal ganglion cells. J. Neurosci *11*, 1440–1457.

O'Keeffe, G.W., Gutierrez, H., Pandolfi, P.P., Riccardi, C., and Davies, A.M. (2008). NGF-promoted axon growth and target innervation requires GITRL-GITR signaling. Nat. Neurosci. *11*, 135–142.

O'Neill, K.M., Akum, B.F., Dhawan, S.T., Kwon, M., Langhammer, C.G., and Firestein, B.L. (2015). Assessing effects on dendritic arborization using novel Sholl analyses. Front. Cell. Neurosci. *9*, 285.

Packer, A.M., McConnell, D.J., Fino, E., and Yuste, R. (2013). Axo-dendritic overlap and laminar projection can explain interneuron connectivity to pyramidal cells. Cereb. Cortex *23*, 2790–2802.

Peng, Y., Lee, J., Rowland, K., Wen, Y., Hua, H., Carlson, N., Lavania, S., Parrish, J.Z., and Kim, M.D. (2015). Regulation of dendrite growth and maintenance by exocytosis. J. Cell Sci. *128*, 4279–4292.

Radojević, M., and Meijering, E. (2017). Automated neuron tracing using probability hypothesis density filtering. Bioinformatics *33*, 1073–1080.

Rajković, K., Marić, D.L., Milošević, N.T., Jeremić, S., Arsenijević, V.A., and Rajković, N. (2016). Mathematical modeling of the neuron morphology using two dimensional images. J. Theor. Biol. *390*, 80–85.

Rall, W. (1957). Membrane time constant of motoneurons. Science *126*, 454.

Rapp, M., Segev, I., and Yarom, Y. (1994). Physiology, morphology and detailed passive models of guinea-pig cerebellar Purkinje cells. J. Physiol. *474*, 101–118.

Rekha, J., Veena, L.R., Prem, N., Kalaivani, P., Choudhury, R., Alladi, P.A., Agrahari, M., Raju, T.R., and Kutty, B.M. (2011). NIH-3T3 fibroblast transplants enhance host regeneration and improve spatial learning in ventral subicular lesioned rats. Behav. Brain Res. *218*, 315–324.

Ristanović, D., Milosević, N.T., and Stulić, V. (2006). Application of modified Sholl analysis to neuronal dendritic arborization of the cat spinal cord. J. Neurosci. Methods *158*, 212–218.

Ristanović, D., Milosević, N.T., Stefanović, I.B., Marić, D., and Popov, I. (2009). Cell image area as a tool for neuronal classification. J. Neurosci. Methods *182*, 272–278.

Schoenen, J. (1982). The dendritic organization of the human spinal cord: the dorsal horn. Neuroscience *7*, 2057–2087.

Sholl, D.A. (1953). Dendritic organization in the neurons of the visual and motor cortices of the cat. J. Anat. *87*, 387–406.

Šišková, Z., Justus, D., Kaneko, H., Friedrichs, D., Henneberg, N., Beutel, T., Pitsch, J., Schoch, S., Becker, A., von der Kammer, H., and Remy, S. (2014). Dendritic structural degeneration is functionally linked to cellular hyperexcitability in a mouse model of Alzheimer's disease. Neuron *84*, 1023–1033.

Smith, T.G., Jr., Marks, W.B., Lange, G.D., Sheriff, W.H., Jr., and Neale, E.A. (1989). A fractal analysis of cell images. J. Neurosci. Methods *27*, 173–180.

Snider, J., Pillai, A., and Stevens, C.F. (2010). A universal property of axonal and dendritic arbors. Neuron *66*, 45–56.

Spruston, N. (2008). Pyramidal neurons: dendritic structure and synaptic integration. Nat. Rev. Neurosci. *9*, 206–221.

Stanko, J.P., Easterling, M.R., and Fenton, S.E. (2015). Application of Sholl analysis to quantify changes in growth and development in rat mammary gland whole mounts. Reprod. Toxicol. *54*, 129–135.

Stepanyants, A., Hirsch, J.A., Martinez, L.M., Kisvárday, Z.F., Ferecskó, A.S., and Chklovskii, D.B. (2008). Local potential connectivity in cat primary visual cortex. Cereb. Cortex *18*, 13–28.

Sümbül, U., Song, S., McCulloch, K., Becker, M., Lin, B., Sanes, J.R., Masland, R.H., and Seung, H.S. (2014). A genetic and computational approach to structurally classify neuronal types. Nat. Commun. *5*, 3512.

Teeter, C.M., and Stevens, C.F. (2011). A general principle of neural arbor branch density. Curr. Biol. *21*, 2105–2108.

Vetter, P., Roth, A., and Häusser, M. (2001). Propagation of action potentials in dendrites depends on dendritic morphology. J. Neurophysiol. *85*, 926–937.

Vuksic, M., Del Turco, D., Vlachos, A., Schuldt, G., Müller, C.M., Schneider, G., and Deller, T. (2011). Unilateral entorhinal denervation leads to long-lasting dendritic alterations of mouse hippocampal granule cells. Exp. Neurol. *230*, 176–185.

Wen, Q., and Chklovskii, D.B. (2008). A cost-benefit analysis of neuronal morphology. J. Neurophysiol. *99*, 2320–2328.

Wen, Q., Stepanyants, A., Elston, G.N., Grosberg, A.Y., and Chklovskii, D.B. (2009). Maximization of the connectivity repertoire as a statistical principle governing the shapes of dendritic arbors. Proc. Natl. Acad. Sci. USA *106*, 12536–12541.

Williams, P.A., Thirgood, R.A., Oliphant, H., Frizzati, A., Littlewood, E., Votruba, M., Good, M.A., Williams, J., and Morgan, J.E. (2013). Retinal ganglion cell dendritic degeneration in a mouse model of Alzheimer's disease. Neurobiol. Aging *34*, 1799–1806.

Wilson, M.D., Sethi, S., Lein, P.J., and Keil, K.P. (2017). Valid statistical approaches for analyzing sholl data: Mixed effects versus simple linear models. J. Neurosci. Methods *279*, 33–43.

Wu, C.C., Reilly, J.F., Young, W.G., Morrison, J.H., and Bloom, F.E. (2004). High-throughput morphometric analysis of individual neurons. Cereb. Cortex *14*, 543–554.

STAR★METHODS

KEY RESOURCES TABLE

REAGENT or RESOURCE	SOURCE	IDENTIFIER
Deposited Data		
Morphologies analyzed	https://www.treestoolbox.org/ and https://github.com/cuntzlab/treestoolbox	"Dissecting Sholl analysis into its functional components"
Software and Algorithms		
MATLAB	Mathworks, Inc (https://www.mathworks.com/)	N/A
Trees Toolbox Package	Hermann Cuntz (https://www.treestoolbox.org/download.html)	N/A
Methods S1: MATLAB Trees Toolbox functions and morphologies	"Dissecting Sholl analysis into its functional components"	N/A

CONTACT FOR REAGENT AND RESOURCE SHARING

Further information and requests for resources should be directed to and will be fulfilled by the Lead Contact, Alex D. Bird (bird@fias.uni-frankfurt.de).

METHOD DETAILS

Numerical integrals

Predicting the SIP from the dendrite spanning field required computing multi-dimensional integrals over often complicated domains (Equations 1, 2, and 6). To accomplish this efficiently, a straightforward Monte Carlo integration scheme is used. A large number (10^6) of points are uniformly randomly distributed at each radius and the proportion of points that lie within the domain $\mathbb{D}$ is determined. This proportion is weighted by the arc length (r for planar neurons) or surface area (r^2 for three-dimensional neurons) at that radius.

Quantifying error

To quantify the predictive power of the spanning field method for different dendritic classes, the normalized root-mean-square deviation is used. If the dendrite reaches a maximum euclidean distance of R from the soma and the normalized observed and predicted SIPs are given by $s(r)$ and $s_p(r)$ respectively (where s_p is either the domain-based prediction s_d or the root angle-based prediction s_r), the error E is given by

$$\epsilon = \sqrt{\int_0^R (s(r) - s_p(r))^2 dr} \qquad \text{(Equation 7)}$$

In practice the integral is usually discretised over 25 steps.

Bounding non-convex dendrites

When applying the prediction to non-convex dendrite spanning fields, in particular in three dimensions, it is important to define the correct boundary to the spanning field (Figure 1). This is governed by both the dendrite and the optimal shrink factor s^* (Figure S2A): a parameter that ranges from 0 (convex hull) to 1 (the tightest boundary that produces a connected region).

The shrink factor follows from the topological concept of α-shapes (Edelsbrunner et al., 1983). An α-shape is a generalisation of the convex hull of a point set whereby a boundary is a set of simplices (lines in R^2 and triangles in R^3) constructed by placing discs (or balls in R^3) of radius $1/\alpha$ over the point set so that all points are contained within the disc and the vertices of the bounding simplex lie on the edge of the disc. To enable this construction, α must lie between 0 and some small positive value (the generalisation to negative α values is not necessary here), but small changes in α do not necessarily lead to distinct α-shapes. An α-spectrum is constructed as the set of α-intervals which define distinct boundaries and the shrink factor defines the proportion of the way through this spectrum that an α value is chosen. In practice this procedure is implemented through the MATLAB *boundary* function.

For many dendrites, the convex hull does not represent the actual spanning field, while a shrink factor of 1 gives over-fitted boundaries for planar neurons (Figure S2B) and can lead to wholly unrealistic domains in three dimensions (Figure S2C). To assign the most appropriate shrink factor, s^*, to a dendritic field, it is necessary to develop a metric that approximates how well a particular boundary captures the true shape of the dendrite.

We take the set of terminal dendritic points and see what proportion of the direct paths between them lie entirely within the tightest boundary (a shrink factor of 1) that contains all termination points. For a convex hull, all such paths would lie within the boundary and so this measure gives the relative difference between the two extreme shrink factors. We refer to this value, between 0 and 1 as the convexity (where 1 gives an entirely convex neuron). The optimal shrink factor s^* is defined as one minus the convexity and for most dendrites this lies in the range of 0 to 1; although note also that small changes in shrink factor do not typically have a large effect on the error of the SIP prediction (Figure S2D). The distribution of convexities for different classes of neuron is plotted in in Figure S2E and tabulated in Table S1; many cell classes have fairly small and often distinct ranges of convexities.

A MATLAB Trees Toolbox function *convexity_tree* to compute the convexity of a tree is included in Methods S1: MATLAB Trees Toolbox functions and morphologies.

Calculating root angles for reconstructed morphologies

The root angle distribution for a given cell is computed using a custom function. The dendritic arbor is resampled into segments 1 μm in length using the existing *resample_tree* function. Each 1 μm segment is assumed to be straight (higher sampling frequencies can be used for especially tortuous dendrites) and has a 'parent' and a 'child' point in R^3, where the parent point is more proximal to the soma by path length and the child is more distal (see Cuntz et al. (2010), for a full discussion). For each segment the angle between the vector from the child to the parent and the vector from the child directly to the soma is calculated using Equation 3.

A MATLAB Trees Toolbox function *rootangle_tree* to compute this distribution is included in Methods S1: MATLAB Trees Toolbox functions and morphologies.

Defining basal, apical trunk, and apical tuft dendrites on a pyramidal cell

Pyramidal neurons, specifically in this study cortical layer V and hippocampal CA1 pyramidal neurons, have dendrites that are divided into basal and apical sections with potentially distinct functional roles (Spruston, 2008). Sholl analysis is often applied separately to the basal and apical dendritic trees of pyramidal neurons to reflect this (Sholl, 1953; Johnson et al., 2016; Keil et al., 2017), with the primary branch of the apical trunk used as the center of measurement for the apical section. To replicate this analysis for large numbers of cells, we developed a simple algorithm to label the primary branch point of the apical tree.

While basal and apical sections are often labeled during reconstruction, this is not always the case and the apical tuft is almost never distinct from the main apical trunk. To identify the apical trunk if the reconstruction is not labeled, the dendritic branch leaving the soma with the greatest total length of dendrite connected to it is selected. To identify the primary branch point, the bifurcation closest to the soma (by path length) such that at least 15% of total dendritic length lies distal (in terms of path length) to each branch is selected. If no such bifurcation exists, the threshold is lowered to 0.9 times its previous value and so on until the primary branch point is located. This procedure reliably identifies the major branch point at the top of the apical trunk (Figure S5). The synthetic $bf = 0$ layer V pyramidal morphology in Figure 6D has an apical tree that is generated by a pure minimum spanning tree algorithm (Cuntz et al., 2010); in this extreme case the process described here does not identify a major branch point and it was necessary to pick an appropriate point manually.

Analytical form of root angle distribution

The root angle distribution in an idealized domain is modeled as a modified von Mises distribution (Forbes et al., 2011). The distribution depends on a single variable κ, with increased κ giving a stronger centripetal bias. For planar neurons, the von Mises root angle distribution $f_{r,2}(\theta_r)$ is given by

$$f_{r,2}(\theta_r) = \frac{e^{\kappa \cos(\theta_r)}}{\pi I_0(\kappa)} \quad \text{(Equation 8)}$$

where $I_0(\kappa)$ is the 0^{th}-order modified Bessel function and the domain is $[0, \pi]$. κ controls the spread of the distribution; $\kappa = 0$ gives a uniform distribution with no angular preference and $\lim_{\kappa \to \infty}$ gives a delta function at the origin where all dendritic segments point directly to the soma. For larger values of κ, the von Mises distribution can be approximated by a half normal distribution with standard deviation $\sigma = \kappa^{-(1/2)}$.

To infer the root angle distribution in three dimensions, it is necessary to incorporate the spherical area element at a given root angle θ_r, which decreases for smaller root angles. The von Mises root angle distribution $f_{r,3}(\theta)$ for $0 \leq \theta \leq \pi$ is

$$f_{r,3}(\theta_r) = \frac{\kappa \sin(\theta_r)\, e^{\kappa \cos(\theta_r)}}{2 \sinh(\kappa)} \quad \text{(Equation 9)}$$

These are plotted in Figure 3B.

Linking root angle to balancing factor

It is possible to map the balancing factor *bf* between short cable lengths and short conduction times (Cuntz et al., 2010) to the centripetal angle distribution. The balancing factor is used to generate synthetic morphologies and is independent of the spanning domain $\mathbb{D}$ and the density of neuronal target points while the root angle distribution f_r does depend on both of these factors but

is a metric that can be calculated precisely from a given dendrite. To quantify the form of the relationship between the root angle distribution and the balancing factor, we can generate generalized minimum-spanning trees in different domains in R^2 and R^3 and compute the centripetal bias parameter κ from the von Mises model of their root angle distributions (Equations 8 and 9). This is plotted in Figure S3A for synthetic dendrites bounded by a circle, a square, and an equilateral triangle (of equal area) in R^2 and by a sphere, a cube, and an equilateral cone (of equal volume) in R^3.

Figure S3 plots the relationship between balancing factor *bf* and centripetal bias κ in these domains (black icon). The relationship is roughly exponential, and can be fitted by a function of the form

$$\kappa(bf) = p_1\left[\frac{1}{(1-bf)^{p_2}} - 1\right]^{p_3} \quad \text{(Equation 10)}$$

where the same parameters $p_{1,2,3}$ can be fitted to all three domains in each of R^2 and R^3, and the form of the equation is inspired by an inverted generalized logistic function. If the fit is restricted to the range of balancing factors $[0, 0.8]$ (dashed line in Figure S3A) that encompasses most real neurons (Cuntz et al., 2010, 2012), the parameters (with 95% confidence intervals) are: R^2 $p_1 =$ 1.201 (1.19, 1.212,), $p_2 = 4.39$ (4.299, 4.482), and $p_3 = 0.2857$ (0.2814, 0.29), R^3 $p_1 = 0.7331$ (0.7181, 0.748), $p_2 = 3.714$ (3.568, 3.86), and $p_3 = 0.3331$ (0.3245, 0.3417). The fits are shown in Figure S3A as solid lines.

Using these fits, it is possible to estimate the balancing factor *bf* of a reconstructed neuron with the centripetal bias κ as a sufficient metric. Figure S3B shows the distributions of fitted balancing factors for the morphologies used in this paper. The fitted values for the different cell classes are in agreement with previous results (Cuntz et al., 2010, 2012) and this technique represents a powerful new way to derive a key morphological parameter. A MATLAB Trees Toolbox function *bf_tree* to estimate the balancing factor of a tree from the root angle distribution is included in Methods S1: MATLAB Trees Toolbox functions and morphologies.

The density of the root angle distribution as a function of radius

The von Mises distribution (Equations 8 and 9) or an empirical root angle distribution f_r can be used to define a shape ϕ in R^2 where the radius at an angle θ is given by $f_r(\theta)$ (Figure 5A). This shape is obtained from the raw root angle distribution for planar neurons or by the root angle distribution divided by a factor of $(2\pi\sinh(\kappa)I_0(\kappa)/\kappa\sin(\theta))$ for three dimensional neurons to correct for the spherical area elements. The shape ϕ is stretched by the estimated mean branch length $\sqrt{3\pi V}/2\sqrt{L}$ (where <I>V</I> is the volume of $\mathbb{D}$), predicted from optimal wiring and minimum spanning trees (Cuntz et al., 2012), and convolved with the domain based SIP estimate $s_d(r)$ to produce the corrected estimate $s_r(r)$ (Equation 6). Even in the case that a root angle distribution is given exactly by the von Mises model it is not possible to define the shape analytically in the correct coordinate system, so this is done numerically.

Sholl-based metrics

In the Results and Figure 5 we compare the predicted values of several widely used Sholl-based metrics to those computed from the observed SIP.

Centre of mass The center of mass is the mean distance of dendritic branches from the soma (or apical trunk in the case of pyramidal cell tuft dendrites). The center of mass of *s* is given by the ratio of integrals $(\int_0^R rs(r)dr / \int_0^R s(r)dr)$ and is also discussed in 'Limitations of the dendrite spanning field'.

Critical value and dendrite maximum The critical value is the radius at which most dendrite can be found (i.e., $\mathrm{argmax}(s(r))$) and the dendrite maximum is the value of the SIP here (ie $\max(s(r))$).

Sholl regression coefficients The Sholl regression coefficients k_1 and k_2 quantify the changing density of dendrite moving away from the soma. k_1 is the semilog regression coefficient which is used to discriminate different neurons with short, complex dendrites and k_2 is the loglog regression coefficient which is more appropriate for long dendrites with little branching. The coefficients are fitted to the equations

$$\log_{10}\left(\frac{s(r)}{\pi r^2}\right) = -k_1 r + c\ ,\ \log_{10}\left(\frac{s(r)}{\pi r^2}\right) = -k_2\log_{10}(r) + c \quad \text{(Equation 11)}$$

for planar neurons. For three dimensional cells, the denominators of the arguments of the logarithms are replaced by $(4/3)\pi r^3$.

Ramification and branching indices Ramification and branching indices take another approach to the SIP and seek to quantify how often a dendrite branches. The Schoenen ramification index (Schoenen, 1982) divides the dendrite maximum by the number of primary branches leaving the soma. The branching index <I>BI</I> Garcia-Segura and Perez-Marquez (2014) is better able to distinguish different SIPs and is given by

$$BI = \sum_n \max(r_n(s(r_n) - s(r_{n-1})), 0) \quad \text{(Equation 12)}$$

where $r_{0,1,\ldots}$ is a discretisation of [0,R] and only positive summands are considered (as shown by the max function). The version used here differs slightly from that defined in Garcia-Segura and Perez-Marquez (2014) where r_n is taken as an index rather than a radius; as we consider cell classes over a range of different scales, taking r_n as a radius gives greater meaning to the *BI*.

Electrotonics and compartmentalisation

For Figure 6D passive electrotonic properties of axial resistivity 100 Ωcm and membrane conductivity 5×10^{-5} S/cm^2 were assigned to the pyramidal cells. The electrotonic signature, the set of transfer resistances from each node to all other nodes, was computed using the existing Trees Toolbox function *sse_tree* (Cuntz et al., 2010). The compartmentalisation was defined by assigning a threshold value, in this case 0.13995, and finding the regions of the tree within which voltages do not attenuate below this proportion of the maximum input resistance. Different thresholds would lead to different numbers of compartments in a given dendrite.

Morphologies used in figures

This paper analyses cellular morphologies reconstructed from a very wide array of animal species, brain regions, and experimental laboratories. For completeness we record the data used here when morphologies are shown in Table S2. In Figure 6, two sets of artificial cortical pyramidal cell morphologies, generated using a generalized minimum spanning tree algorithm are shown and analyzed. The layer V morphologies are taken directly from examples in Cuntz et al. (2010, Figure 7 in that paper). The layer II/III pyramidal cells were generated using the procedure described in Cuntz (2012) and Mazzoni et al. (2015). Briefly, straight axonal segments were randomly generated in distinct layers corresponding roughly to cortical layers II/III and I (light and dark green respectively in Figure 6E) and dendrites were connected to the axons in such a way as to minimize the total and path lengths of each dendritic tree (the balancing factor $bf = 0.7$). Axons were distributed isotropically within planes perpendicular to the cortical column at uniform random depths. The apical dendrites, connecting to axons in layer I were generated before the basal dendrites.

Appendix 1

Inferring the root angle distribution

The root angle distribution is straightforward to compute with a full reconstruction of the neuron. A major advantage of the techniques presented here, however, is to allow properties of the neuron to be discerned from limited or noisy data. The centripetal bias κ of a neuron can be reliably estimated from relatively few independent samples.

A bayesian approach to estimating κ (given that the von Mises model is appropriate for a given class of neuron) allows the uncertainty in centripetal bias to be quantified. The conjugate prior $\Pi[\kappa]$ for the von Mises distribution is widely known (Gutthorp and Lockhart, 1988) and can be applied directly in the case of planar neurons, giving a posterior of the form

$$\Pi_2[\kappa \mid \theta_{i=1\ldots n}] \propto \frac{e^{\kappa R_0}}{(\mathrm{I}_0(\kappa))^c} \qquad \text{(Equation 13)}$$

with hyperparameters $R_0 = \sum_{i=1}^{n} \cos(\theta_i)$ and $c = n$. Figures S4A and S4B show this distribution for different numbers of samples from a cerebellar Purkinje cell and tangential HS cell respectively.

In three dimensions, the conjugate prior can be derived in a similar way, giving a posterior of the form

$$\Pi_3[\kappa \mid \theta_{i=1\ldots n}] \propto \frac{\kappa^c e^{R_1 + \kappa R_0}}{\sinh^c(\kappa)} \qquad \text{(Equation 14)}$$

with hyperparameters $R_0 = \sum_{i=1}^{n} \cos(\theta_i)$, $R_l = \sum_{i=1}^{n} \log(\sin(\theta_i))$, and $c = n$. Figures S4C and S4D show this distribution for different numbers of samples from a dentate gyrus granule cell and the basal dendrites of a cortical Layer V pyramidal cell respectively.

Appendix 2

Analytical chloanges in SIP

The three components of the SIP can be considered analytically in a toy model (Figure S6). Consider a dendritic tree of length $L_d = 7.5$mm, no centripetal bias $(\kappa = 0)$, and bounded by a spherical domain of radius $R = 100\mu$m. Then the SIP given by Equations 1 and 5 reduces to

$$s_r(r) = \frac{3L_d}{2R^3} r^2 \qquad \text{(Equation 15)}$$

for $0 < r < R$ and $s_r(r) = 0$ otherwise. This is the blue curve in the top-left corner of Figure S6. We consider the effect on this curve from manipulating the size and shape of the spanning domain $\mathbb{D}$ and the centripetal bias κ.

Size of spanning field

A change in the scale of the neuron can be seen by increasing the extent of the scanning field R and the total dendritic length L_d (Figure S6, vertical). We decrease the density of dendritic cable with the increasing volume of the spanning domain such that there is a -0.55 power relationship between the two as observed for many real dendrites by Teeter and Stevens (2011). The reduction in density has the effect of reducing the dendrite maximum and increasing the expected mean branch length.

Shape of spanning field

A change in the spanning domain of a neuron can indicate a substantial reduction in connectivity and functionality (Figure S6, horizontal). This type of change can be reproduced in this simple model by changing the spanning domain from a sphere to an ellipsoid.

If the boundary of the domain $\mathbb{D}$ is an ellipsoid given in cartesian coordinates by $R^2 = x^2 + y^2 + \epsilon z^2$, then increasing the parameter E above 1 flattens the initial sphere along its z axis. In this case the SIP can be written as

$$s_r(r) = \begin{cases} \frac{3\epsilon^{0.55} L_d r^2}{2R^3} & \text{if } r \leq \frac{R}{\sqrt{\epsilon}} \\ \frac{3\epsilon^{0.55} L d}{2R^3} r \sqrt{\frac{R^2 - r^2}{\epsilon - 1}} & \text{otherwise} \end{cases} \quad \text{(Equation 16)}$$

where the density of dendritic cable has been increased to match the reduced volume of the spanning domain using the relationship given in Teeter and Stevens (2011). The changed shape of the spanning domain has a large effect on the form of the SIP, while the increased dendritic density reduces the expected mean branch length.

Centripetal bias

A difference in centripetal bias changes the root angle distribution and can indicate a changed weighting between total length and synaptic delays or accompany a loss in dendritic density (Figure S6, different colors). In Equation 15, this can be reproduced by increasing κ. The final SIPs with centripetal bias $\kappa > 0$ in Figure S6 are obtained by convolving the domain based predictions (Equations 15 and 16) with the root angle distribution (Equation 9) scaled by the mean branch length, which depends on the density of dendrite. This means that the effect of the convolution can be different in the different domains. Note also that the SIPs with centripetal bias are scaled up by a factor of $(2/\pi)(1 + (\tanh(-\kappa/2)/\kappa))$ to account for the increased influence of radially aligned dendritic segments on the ratio between total length L_d and the integral of the SIP (Equation 5).

Increasing the centripetal bias shifts the mass of the SIP toward the soma and smooths the edge effects of the boundary. It also causes an increase in the integral A_s of the SIP for a given total dendritic length L_d.

QUANTIFICATION AND STATISTICAL ANALYSIS

The goodness-of-fit of the von Mises model to the root angle distributions of different cell classes in Table S1 is quantified using the R^2 coefficient of determination. The *p-value*s quoted in 'Alzheimer's in hippocampal CA1 pyramidal cells' come from the distribution of the sample mean assuming a von Mises distribution.

DATA AND SOFTWARE AVAILABILITY

Neuronal morphologies were evaluated using the freely available Trees Toolbox package (Cuntz et al., 2010) for MATLAB. True SIPs $s(r)$ were computed using the existing *sholl_tree* function. The full set of morphologies used in this paper is included in the Trees Toolbox format as a MATLAB workspace as Methods S1: MATLAB Trees Toolbox functions and morphologies, related to STAR Methods. Most morphologies were taken from the NeuroMorpho database (Ascoli et al., 2007); the dentate gyrus granule cells and hippocampal CA1 pyramidal cells used in Figure 6 are taken from Vuksic et al. (2011) and Šišková et al. (2014) respectively.

Cell Reports, Volume *27*

Supplemental Information

Dissecting Sholl Analysis into Its Functional Components

Alex D. Bird and Hermann Cuntz

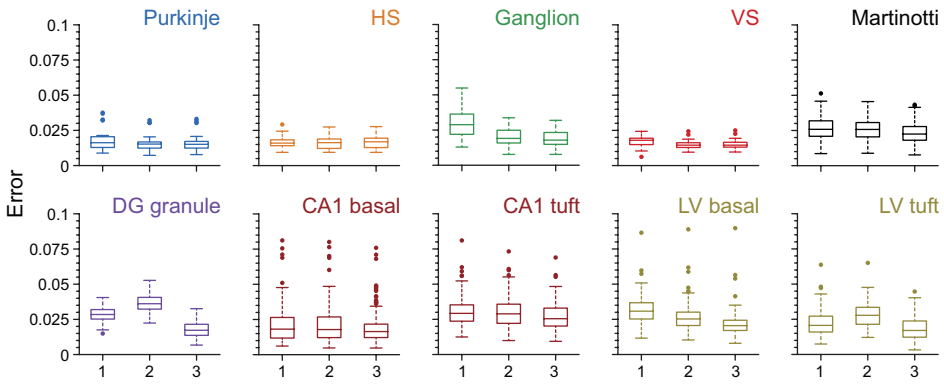

Fig S1. Related to Figure 1: Distribution of estimation errors for the different cell classes used in the paper. Errors (Eq 7) are (from left to right) in the convex domain-based prediction (Eq 1), the fitted domain-based prediction (Eq 1 with $\mathbb{D}$ defined in Methods), and the root angle based prediction (Eq 6). The number of cells of each type is given in Supplementary Table 1.

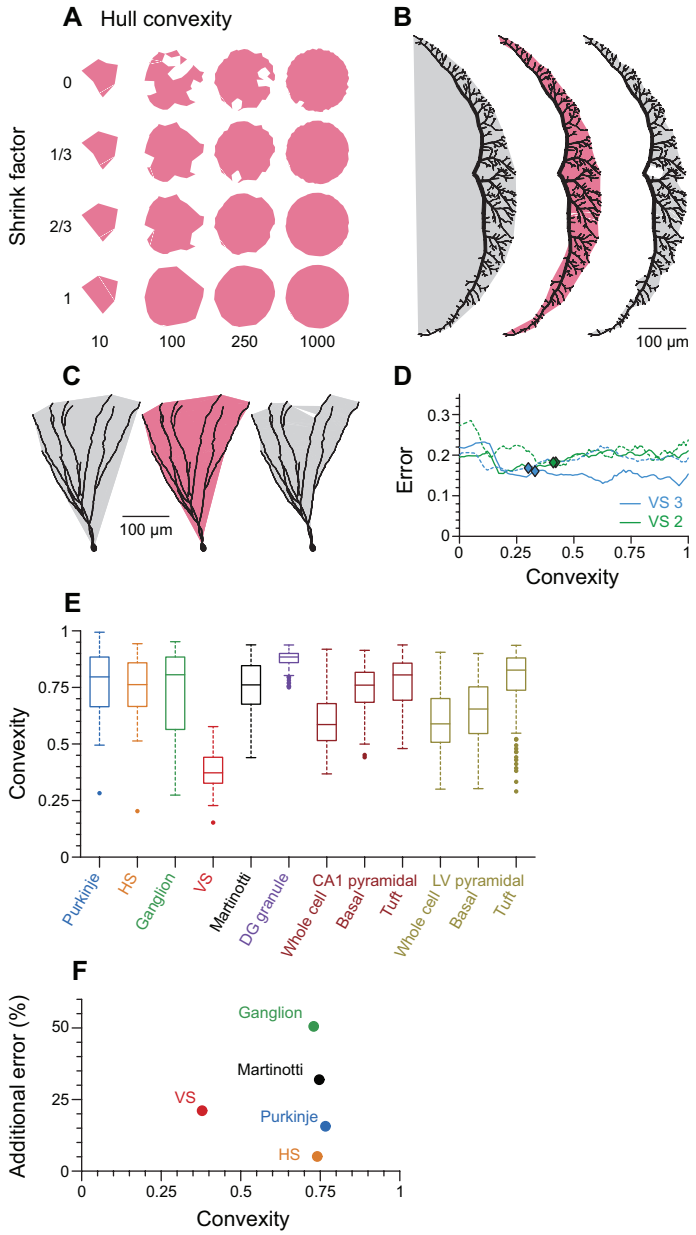

Fig S2. Related to Figure 1: Defining the dendrite spanning field for non-convex dendrites. **a** Illustration of different shrink factors (vertical axis) applied to sets of different numbers of points (horizontal axis) uniformly distributed in a disc in $\mathbb{R}^2$. **b** Illustration of different shrink factors (0, $s*$, and 1, shaded areas) from left to right applied to a blowfly VS type 1 tangential neurons (Cuntz et al, 2008). **c** Illustration of different shrink factors (0, $s*$, and 1, shaded volumes) from left to right applied to a mouse cerebellar dentate gyrus granule cell (Beining et al, 2017). **d** Error (Eq 7) in the domain-based estimation as a function of bounding shrink factor for two type 2 VS tangential cells (green lines) and two type 3 VS tangential cells (blue lines). The fitted shrink factors $s*$ are shown with diamonds of the appropriate colour. **e** Distribution of convexities for different cell classes. **f** Percentage additional mean-squared error of normalised SIP (Eq 7) as a function of convexity (see Methods) for different cell classes. Higher values mean that the convex hull provides a worse boundary. The number of cells of each class is given in Table S1.

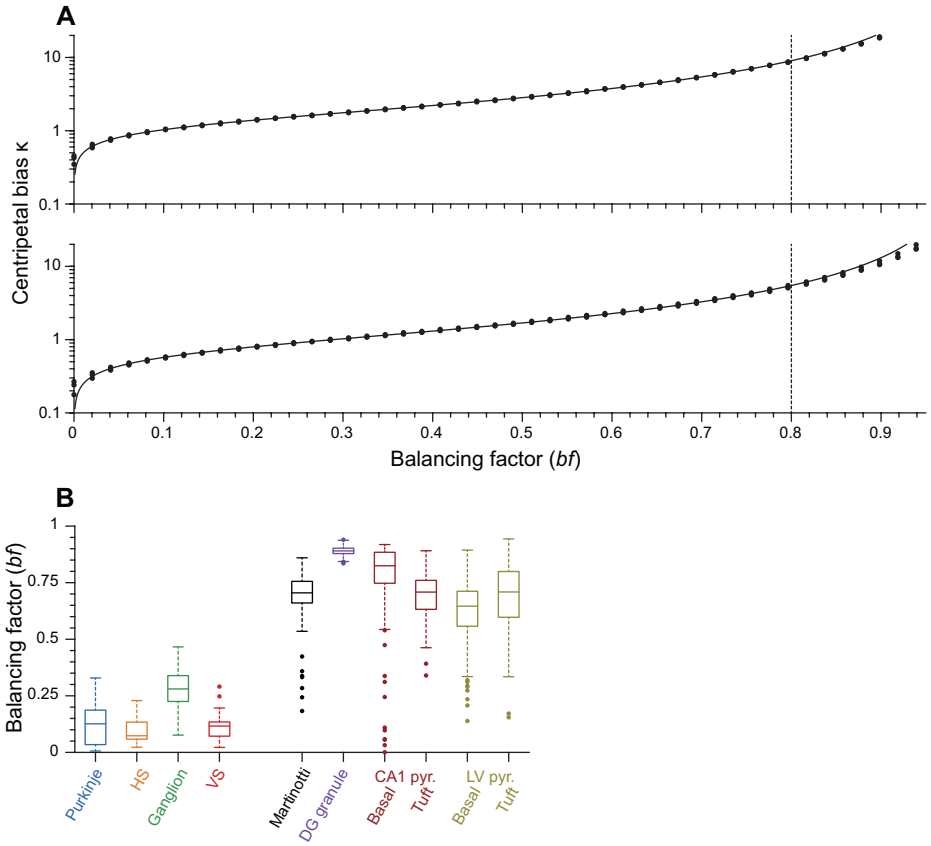

Fig S3. Related to Figure 3: Relating balancing factor bf to centripetal bias κ. a Centripetal bias κ as a function of balancing factor bf for different shapes in $\mathbb{R}^2$ (top) and $\mathbb{R}^3$ (bottom). Numerical results are given as black shapes (circles, squares, and triangles correspond respectively to circular, square, and triangular boundaries in $\mathbb{R}^2$ and to spherical, cubic, and conical boundaries in $\mathbb{R}^3$); the fits under Eq 10 are given by the solid line with parameters described in Methods. **b** Distributions of balancing factors bf for different cell classes estimated from the root angle distribution. The number of cells of each class is given in Table S1.

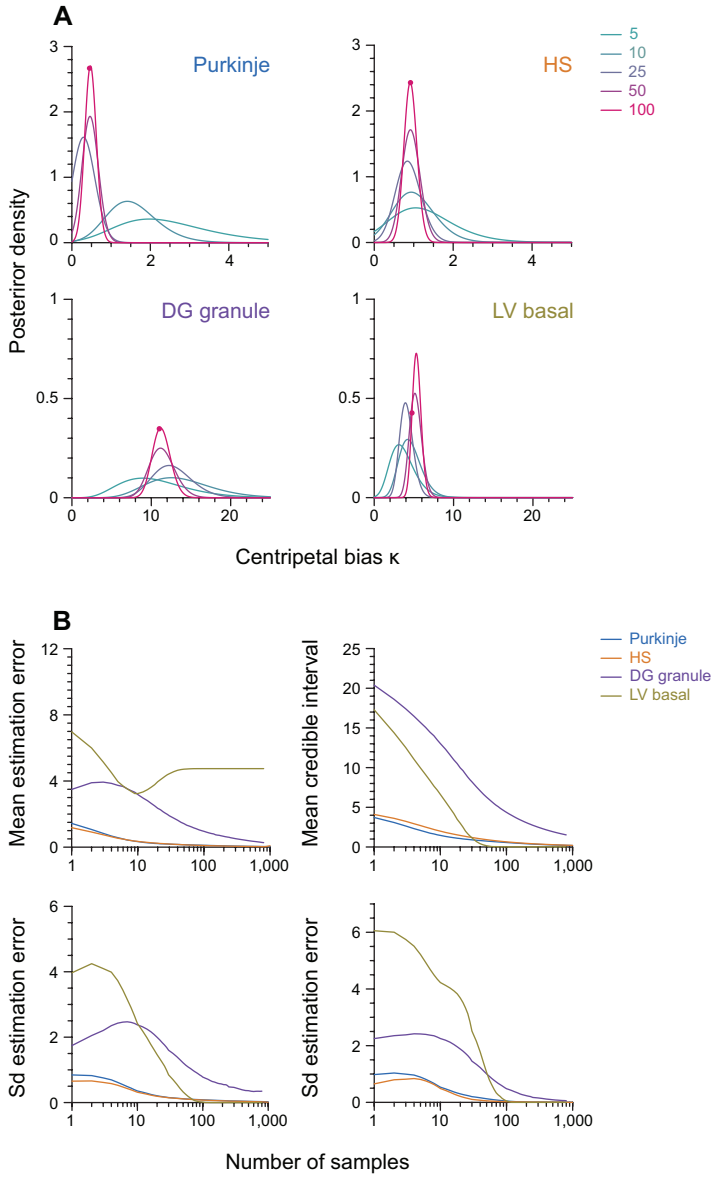

Fig S4. Related to Figure 3: Inferring centripetal bias. **a** Example posterior distributions for the centripetal bias parameter κ after different numbers of independent samples from reconstructed dendrites. Clockwise from top left the dendrites are a cerebellar Purkinje cell, a tangential HS cell, the basal dendrites of a cortical layer V pyramidal cell, and a dentate gyrus granule cell. The maximum likelihood estimate of κ from the entire cell is indicated in each panel by a dot on the 100 sample posterior distribution. **b** Top left: The mean estimation error for κ as a function of the number of samples. Bottom left: The standard deviation in estimation error for κ as a function of the number of samples. Top right: Width of the 95% credible interval for κ as a function of the number of samples. Bottom right: The standard deviation in the width of the 95% credible interval for κ as a function of the number of samples. Each plot shows the values for an example cell of each of the four types above

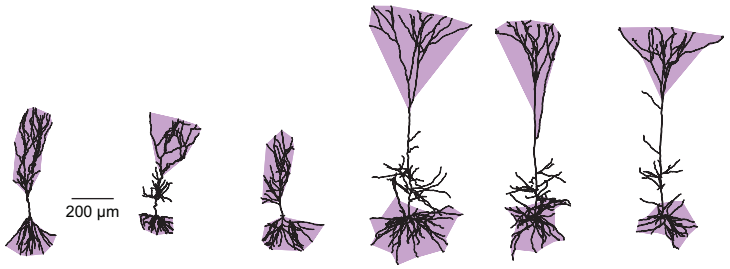

Fig S5. Related to Figure 5: Automated sorting of pyramidal cells into basal, apical trunk and apical tuft regions. Selection of 3 hippocampal CA1 (left) and three cortical Layer V (right) pyramidal cells sorted into basal and apical tuft segments (shaded purple). All dendritic radii increased by $1\mu\mathrm{m}$ for visualisation purposes.

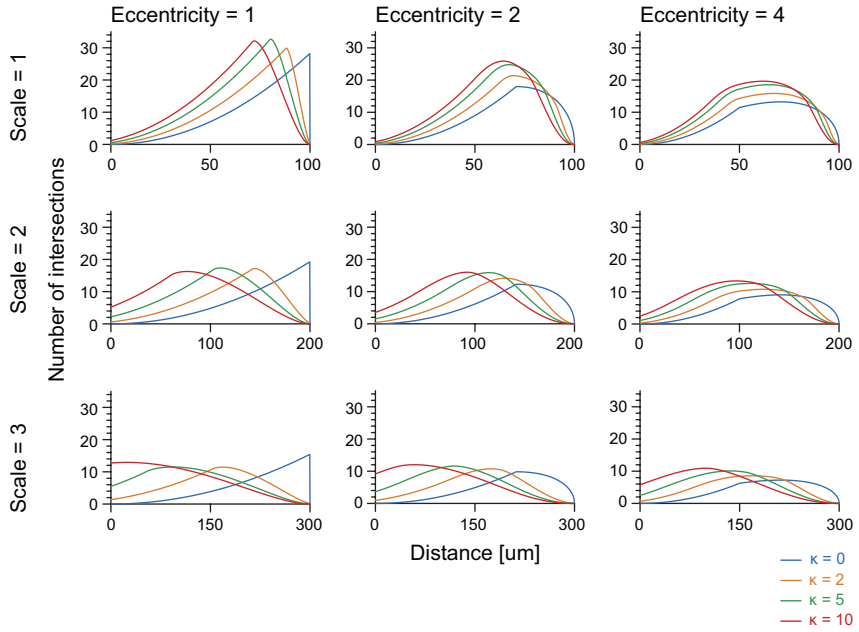

Fig S6. Related to Figure 6: Analytical form of SIP for an idealised domain. Analytical SIPs under Eqs 15 and 16. The domain $\mathbb{D}$ is taken to be a sphere of radius $100\mu\mathrm{m}$, which is scaled up in each dimension by the Scale (vertical direction) and flattened by the $\mathrm{Eccentricity}$ into an ellipsoid along one axis (horizontal direction). For each domain, four different values of centripetal bias κ (0, 2, 5, and 10) are plotted. The density of dendrite is proportional to the volume of the domain to the power -0.55 (see text), and the integral of the SIP follows from Eq 6.

Cell class	Number of cells studied	Convexity	Centripetal bias κ	R^2 value
Cerebellar purkinje	28	0.77 ± 0.17	**0.87** (0.73, 1.00)	0.91
Retinal ganglion	31	0.74 ± 0.16	**0.89** (0.72, 1.06)	0.87
HS	25	0.73 ± 0.19	**1.49** (1.36, 1.62)	0.97
VS	30	0.38 ± 0.10	**0.96** (0.74, 1.17)	0.83
Cortical LV Martinotti	175	0.75 ± 0.11	**3.25** (2.86, 3.64)	0.93
Dentate gyrus granule	242	0.87 ± 0.03	**12.07** (11.29, 12.86)	0.99
Hippocampal CA1 (basal)	161	0.74 ± 0.10	**7.39** (5.89, 8.88)	0.80
Hippocampal CA1 (tuft)	161	0.76 ± 0.13	**3.51** (2.89, 4.13)	0.84
Cortical LV pyramidal (basal)	167	0.65 ± 0.13	**2.69** (2.26, 3.12)	0.86
Cortical LV pyramidal (tuft)	167	0.78 ± 0.14	**3.24** (2.42, 4.07)	0.84

Table S1. Related to Figures 1 to 5. Table of numbers of morphologies of each cell class in the study, with the mean ($\pm$ standard deviation) of the convexity, fitted centripetal biases κ with 95% confidence intervals, and R^2 values for the von Mises model fits.

Figure	Panel	Provenance
	a	Rat cerebellar Purkinje cell NMO_00891 (Vetter et al, 2001).
	b	Guinea pig cerebellar Purkinje cell NMO_00611 (Rapp et al, 1994).
	c	Blowfly *Calliphora Vicina* HS visual neuron NMO_06656; published with the Trees Toolbox (Cuntz et al, 2008).
Figure 1	**d**	Rabbit retinal local projecting ganglion cell NMO_62508 (Guo et al, 2013).
	e	Blowfly *Calliphora Vicina* VS visual neuron NMO_06661; published with the Trees Toolbox (Cuntz et al, 2008).
	f	Blowfly *Calliphora Vicina* VS visual neuron NMO_06671; published with the Trees Toolbox (Cuntz et al, 2008).
	g	Mouse cortical Layer V Martinotti interneuron NMO_60397 (Castillo-Gómez et al, 2015).
	a	Rabbit retinal starburst amacrine cell NMO_00765 (Bloomfield and Miller, 1986).
Figure 2	**b**	Rat cerebellar Purkinje cell NMO_00891 (Vetter et al, 2001).
	c	Rat hippocampal dentate gyrus granule cell NMO_50707 (Beining et al, 2017).
	a	Rat hippocampal dentate gyrus granule cell NMO_50707 (Beining et al, 2017).
Figure 3	**d**	Rat cerebellar Purkinje cell NMO_00891 (Vetter et al, 2001), blowfly *Calliphora Vicina* HS visual neuron NMO_06656; published with the Trees Toolbox (Cuntz et al, 2008), dentate gyrus granule cell as above, and rat hippocampal CA1 pyramidal cell NMO_08608 (Marcelin et al, 2012).
	b	Rat neocortical Layer V pyramidal cell available on ModelDB with Accession no. 13953 (first morphology, Hay et al (2011)).
Figure 5	**c**	Rat hippocampal dentate gyrus granule cell NMO_50707 (Beining et al, 2017).
	d	Rat hippocampal CA1 pyramidal cell NMO_08608 (Marcelin et al, 2012).
	a	Blowfly *Calliphora Vicina* HS lobula plate tangential neuron NMO_06656 (published with the Trees Toolbox, Cuntz et al (2008)) and fruitfly *Drosophila Melanogaster* lobula plate tangential HS neuron NMO_50994 (Cuntz et al, 2013).
Figure 6	**b**	Mouse hippocampal dentate gyrus granule cells with and without perforant path lesion, morphologies from Vuksic et al (2011).
	c	Mouse hippocampal CA1 pyramidal neurons, wild type and in a transgenic model of Alzheimer's disease, morphologies from Šišková et al (2014).

Table S2. Related to all Figures. Table of morphologies shown in each figure in the paper. Where morphologies are downloaded from NeuroMorpho (Ascoli et al, 2007), IDs are provided, otherwise the provenance is described.